Mathematical Modeling, Immersed Boundary Simulation, and Experimental Validation of the Fluid Flow around the Upside-Down Jellyfish *Cassiopea xamachana*

Christina Hamlet

A dissertation submitted to the faculty of the University of North Carolina at Chapel Hill in partial fulfillment of the requirements for the degree of Doctor of Philosophy in the Department of Mathematics.

Chapel Hill
2011

Approved by

Advisor: Professor Laura Miller
Reader: Professor Gregory Forest
Reader: Professor Tyson Hedrick
Reader: Professor William Kier
Reader: Professor Peter Mucha

ABSTRACT

CHRISTINA HAMLET: Mathematical Modeling, Immersed Boundary Simulation, and Experimental Validation of the Fluid Flow around the Upside-Down Jellyfish *Cassiopea xamachana*

(Under the direction of Professor Laura Miller)

The jellyfish has been the subject of extensive research in the areas of ecology, biomechanics, fluid dynamics and engineering. Previous mathematical and experimental studies of the flows generated by jellyfish focused primarily on swimming mechanisms. Recently, the fluid dynamics of feeding from currents generated during swimming has been considered. In this study the benthic lifestyle of the upside- down jellyfish *Cassiopea xamachana* was capitalized upon to explore the fluid dynamics of feeding uncoupled from swimming. A two-dimensional mathematical model was developed to capture the fundamental characteristics of the motion of the unique concave bell shape. Given the prominence of the oral arm array, this structure was included and modeled as a porous layer that perturbs the flow generated by bell contractions. The immersed boundary method was used to solve the fluid-structure interaction problem. Parameter sweeps were used to explore numerically the effects of changes in pulse dynamics and the properties of the oral arms independently. Velocity fields obtained from live organisms using digital particle image velocimetry were used to validate the numerical simulations of the model. Parameter

sweeps were used to explore the effects of scaling and to compare the model to a more traditional bell-only model. The effects of low-velocity background flow, neighboring jellyfish, and synchronous and asynchronous pulsing were also examined. The presence of the prominent porous layer structure in the field of flow increased the flux of new fluid from along the substrate to the bell. A consistent pattern of flow across the porous layer across a wide range of background flow patterns. The numerical simulations showed that pauses between bell expansion and the next contraction altered fluid flow over the bell and through the oral arms. Studies of the effects of neighboring models showed that spacing and relative size of individuals changed flow rates substantially. These substantial changes could explain so-called "hitchhiking" behavior observed in smaller or weakened jellyfish.

ACKNOWLEDGMENTS

I count myself lucky to have had so much support from so many people on my journey. I owe each one here and a number of other people a debt of gratitude for any success I have enjoyed in my life. Laura Miller has been a terrific advisor, mentor, and friend. I have been lucky to work under a person that takes a genuine interest in the progress and success of her students. She constantly encouraged research, publications and presentations and provided the support needed to ensure the endeavors were successful. Her perspective is unique and her innovation is inspiring. The many conversations I have had with her have helped to shape my perspectives as a scientist, a researcher and an academic. She always welcomes opinions and questions, no matter how wrong it turned out I was. I admire her for navigating the sometimes difficult waters of interdisciplinary research in the pursuit of scientific knowledge.

Thanks to my committee Greg Forest, Ty Hedrick, Bill Kier, and Peter Mucha, for the many conversations about my project, research, career guidance, publishing, and becoming confident in my work. Each one of them is an amazing scientist in their own right and I am grateful for their insight and support. My graduate work was partially funded by Laura Miller's Burroughs Wellcome Fund (BWF CASI ID 1005782.01) as well as a collaborative NSF-FRG Grant No 0854961 headed by Michael Minion. My thanks for this generous support. I also thank David Adalsteinsson not only for his patience and diligence as a teacher but also for his generosity in allowing me to use DataTank freely

to complete my graduate work. His incredible program has been an invaluable tool in my research.

I have enjoyed the support of my family and also of friends. My thanks to my parents, as well as to my brother and sister-in-law and their three terrific kids for all of the support I've received from them over the years. Arvind Santhanakrishan's terrific work obtaining PIV data served to drive a number of research projects including some of those presented here. Thanks also to Walt Rogers, Megan Gyoerkoe Makani Dollinger, Audrey Lowe and Terry Rodriguez for their hard work in the Math Physiology lab. Terry also was invaluable in working out Matlab routines for the Markov processes used for random pulsing. I owe special thanks to Liz Bouzarth, Amber Sallerson Jackson, Roxana Tiron, and Jennifer Young for guiding a junior graduate student through her first few years. My current and former officemates have been terrific colleagues and friends in every way—Andrea Richmond, Jeanette Olli, Indrani Rao, Mandi Traud, and Lauren Cooper. My thanks to people outside the department who have leant support over the years, including Michael Robeson, Jeff Brown, Darla Eisemann, Dennis Evangelista, and most notably Karin Leiderman Gregg, one of the most insightful and inspirational people I have ever met.

I am eternally indebted to Wanda Strychalski. Wanda was there ready to help a new student learn and thrive in this department. She was by far the best officemate a person could hope to have. Infinitely patient as I sometimes struggled, a terrific person with whom to discuss ideas or to pal around and the undisputed master of all things DataTank. Wanda has been a great collaborator and an even better friend.

Though not well-versed in research, three terrific felines have in many ways been

instrumental in helping me achieve my goals. Although no longer with us, Gandalf was always there with a comforting nudge or a crazy antic to make me laugh. Aizen and Mr. Pibb came to us as rescue kittens and have been a constant source of love, support, and entertainment since the minute we met them.

Words cannot express how much I owe Terry Campbell. For 20 years he has been my best friend. I could not have found a better or more supportive husband and partner in crime. He has encouraged me every step of the way in words, in action, and by example. I am incredibly lucky to have found a partner that complements me in so many ways. An amazing scientist, he has been indispensable in working through ideas, editing papers, and really enjoying science. An even more amazing person, he makes me laugh when I'm down, he always encourages me to pursue my dreams and he never lets me give up. Thank you Terry, I love you. I don't know if it took a miracle, but we've had fun storming the castle.

CONTENTS

LIST OF FIGURES

LIST OF TABLES

CHAPTER 1

Introduction

Jellyfish have been the subject of biomechanical and fluid dynamic research aimed at understanding the nature of unsteady propulsion [**15, 17, 20, 68**]. These studies have focused not only on understanding the mechanisms of unsteady propulsion but also for biologically-inspired design. Recently there has been additional focus on jellyfish feeding mechanisms. Jellyfish have been categorized into two general groups based on feeding strategy: 1) ambush predators that rely on short bursts of fast motion to trap prey and 2) foraging predators that sample for prey as they swim[**11, 12**].

The focus of this study is the feeding mechanism used by a benthic jellyfish *Cassiopea xamachana*. Instead of employing ambush or foraging behavior, these organisms remain inverted on the seafloor, using the pulsing mechanism of their bells to draw fluid toward their feeding appendages for sampling. While previous research has considered the mechanisms of feeding jellyfish, there has been very little study of this unusual mechanism normally employed for swimming.

In this introductory section, previous work on jellyfish dynamics is reviewed, including work that has described, compared and contrasted the feeding strategies of swimming jellyfish. Next the biology and habitat of *C. xamachana* are described emphasizing those aspects of this genus that make it a model organism for this work. Finally the specific modeling strategies and computational methods used for this study are outlined.

1.1. Previous work on jellyfish dynamics

One of the first studies to mathematically model jellyfish propulsion was by Daniel in 1985 [**17**]. Daniel compared the cost of locomotion (rate of energy consumption divided by the product of weight and speed) for unsteady propulsion in hydromedusae to that of

vertebrates of similar body mass. He used balsa wood models and live specimens to calculate forces and oxygen consumption associated with jellyfish propulsion. Daniel found that the cost of the hydromedusae propulsion was nearly an order of magnitude greater than that of comparable vertebrate swimmers reported in the literature. He attributed as much as 25 % of the increased cost to accelerating the added mass of the surrounding fluid. Daniel's results indicated that formation and shedding of vortices cause the actual costs to deviate significantly from those predicted by potential flow theory, suggesting vortex shedding could offset the cost of unsteady propulsion. Unsteady propulsion was still found to be more costly when compared to undulatory swimming and other forms of vertebrate locomotion.

Demont and Gosline [**20**] later modeled the bell of a hydromedusa as a damped harmonic oscillator. They compared work output predicted by their model with that of experimentally measured data and found them to be in good agreement [**19**]. They also showed that hydromedusae tend to drive their bells at resonant frequencies [**20**]. Using their theoretical and experimental results they showed the efficiency of this form of locomotion is dramatically greater when compared to a single contraction at the same deformation rate.

Recently there has been research into the physical constraints on morphological characteristics of free-swimming medusae. Dabiri et al. [**15**] studied the bell morphology of over 600 extant species of medusae and compared the fineness ratio of their bells (ratio of bell height to bell diameter). Based on this ratio, organisms were categorized as prolate (fineness ratio greater than one (1)) or oblate (fineness ratio less than one (1)). Dabiri et

al. [**15**] found that physical constraints on swimming mechanisms divide jellyfish locomotion into two general categories, small jet propelling organisms and individuals with a low fineness ratio that use a paddling mechanism. Their survey of jellyfish specimens indicated there is a narrow range of observed fineness ratios as the bell diameter increases, indicating there are physical constraints on possible bell morphologies.

Colin and Costello [**11, 12**] studied behaviors and morphological characteristics associated with foraging and other types of feeding behavior. Feeding behaviors are generally categorized as ambush type or foraging type. Ambush predators generally use a pattern of slow cruising until prey is sensed. Then the organism initiates a jet propulsion mechanism through contraction of its bell to move quickly towards the prey. Ambush predators tend to feed on larger organisms than foraging predators. Colin and Costello [**11, 12**] discovered ambush predatory species have very little overlap among them in feeding niches. They also found that ambush predators contract their tentacles while swimming, indicating that swimming and feeding do not generally occur at the same time. Foraging organisms sample the surrounding fluid for prey as they actively or passively swim using the paddling mechanism described above. Cruising and foraging types of feeders experience a great deal of prey overlap and competition among species. In contrast to ambush predators, jellyfish that cruise and swim do not exhibit as clear a pattern of tentacle contraction, indicating that feeding occurs during swimming and cruising.

Recently, numerical simulations of swimming jellyfish have been developed. Lipinski and Mohseni [**47**] used finite element methods to solve this fluid-structure interaction problem and suggested that the vortex patterns generated by the bell motion of *Aequora*

victoria, an oblate medusa, draws fluid through its tentacles. They investigated the interaction of the starting and the stopping vortices and how this affected the fluid motion around the organism. A starting vortex is formed during contraction. The oppositely spinning vortex that forms as the bell reverses its motion during expansion the stopping vortex. Lipinski and Mohseni [**47**] found that in the oblate medusa the starting and stopping vortices interact and partially combine to form a slowly spinning and translating vortex that lingers in the tentacle region before being shed. They assert that this enhances the opportunity for nutrient sampling. In the prolate *Sarsia tubulosa* the starting and stopping vortices form at the tips of the bell and inside of the body cavity, respectively, interacting very little. *Sarsia tubulosa* ejects vortex rings far from the bell with little opportunity for localized foraging. Lipinski and Mohseni suggest the difference in the prominence and positioning of tentacles and oral arms in each organism is influenced by the swimming mechanisms employed to enhance foraging success.

There have also been a number of studies focusing on the efficiency of unsteady propulsion and bio-inspired design. Dabiri and his group have used digitial particle image velocimetry (dPIV) and Lagrangian coherent structures (LCS) to characterize the vortex shedding, mixing, and particle capture associated with jellyfish locomotion [**14, 16, 59, 60, 61**]. Lagrangian coherent structure analysis uses finite time Lyapanouv exponents to characterize particle separation and to to identify boundaries on regions of mixing in flow. Peng [**60**] used LCS to study efficiency in jellyfish propulsion. They found there was a larger region of influence than previously thought, and structures in the upstream wake have a significant effect on the organism's downstream wake and swimming efficiency. Dabiri has also proposed a "universal" vortex formation number as

a measure of physical limit on the optimization of propulsion mechanisms [**14**].

Sahin and Mohseni [**67, 68**] used moving boundary simulations and flow visualization to examine vortex formation patterns in oblate and prolate jellyfish. By examining the shedding and pairing of starting and stopping vortices as well as swimming velocity, thrust, and other aspects of efficiency they compared the performance of jetting versus swimming behavior. They found jetting to be effective for rapid motion, but overall more costly and less efficient than paddling.

Most of previous work has focused on fluid dynamic mechanisms such as vortex formation and feeding in the context of a swimming organism. This is because the majority of medusae spend almost all of their time either swimming or cruising. There are some species, such as members of the genus *Cassiopea*, that engage in a more sedentary lifestyle. These animals remain inverted on the bottom and swimming is thus uncoupled from the pulsing mechanism of the bell, allowing analysis of how the bell motion is used for feeding and other types of particle transport.

1.2. *C. xamachana* as a model organism

The genus *Cassiopea* (Cnidaria, Scyphozoa, Rhizostomae) includes jellyfish found throughout the world in shallow, low flow velocity marine environments [**75, 83**]. Although capable of locomotion, the organism spends the majority of its time on the seafloor with the aboral portion of its bell resting on the substrate (Figure 1.1). Cnidarians such as *C. xamachana* that harbor symbiotic zooxanthellae have been shown to be sources of oxygen and sinks of nitrogen and other inorganic nutrients especially in sunlit areas [**83, 84**]. Recent studies have shown that *C. xamachana* may be used as am indicator of

ecosystem health and also to detect the presence of certain pollutants due to the incorporation of trace elements during particle transfer [**75**].

The sedentary lifestyle of *C. xamachana* makes them more dependent than other foraging medusae on the nutrient exchange in their immediate environment. Upside-down jellyfish typically live in areas such as shallow inshore bays, near seagrass beds, and in mangrove swamps that are characterized by low flow velocities. Maximum flow velocities through mangrove swamps may reach up to 0.7 m/s, velocities within densely packed swamps near the sea floor are likely significantly lower, on the order of 1 cm/second or lower ($< O(1)$ cm/s) [**6, 87**]. Given their sedentary behavior and low ambient flow rates, *C. xamachana spp.* rely heavily on bell pulsations to generate flows necessary food capture, oxygen exchange, temperature regulation, incorporation of zooxanthallae, waste elimination, and gamete distribution [**5, 83**].

The mechanism of the bell contraction and expansion that generates flow appears relatively simple, but is the result of a coordinated system of muscles, neurons, and viscoelastic tissue. Contractions are driven by coronal muscles and pinnate radial muscles [**5**]. These muscles are surrounded by an organic matrix called the mesoglea that stores elastic energy generated during contraction. Once the bell musculature relaxes, energy stored in the mesoglea drives expansion.

Like other members of the order Rhizostomae, *C. xamachana* lack tentacles and the four oral lobes are fused over the central mouth of the organism, forming a canal-like system of tiny suctioning mouth-like structures opening along eight branching oral arms as seen in Figure 1.1 [**10, 36**]. Unlike many other medusae that serve as models for locomotion studies, the oral arm structure constitutes a large part of the overall body

of the organism [**5, 16, 17, 18, 20, 47, 66, 68**]. Sampling and capture of zooplankton prey occurs when water is driven over and across the oral arms.

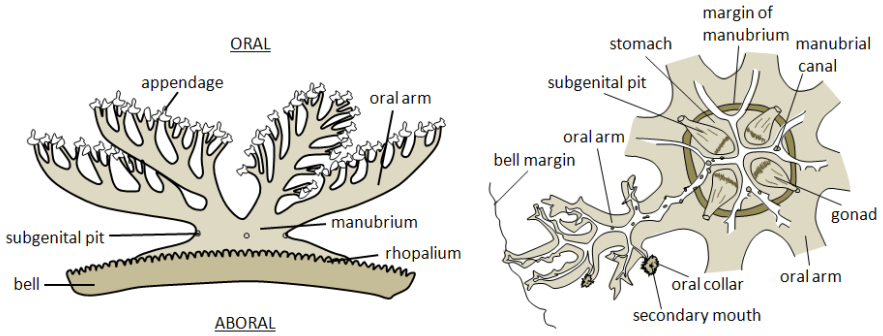

FIGURE 1.1. A diagram showing the main structures of *Cassiopea xamachana* (after Hyman [**36**]). The most salient features for the study are the bell and the oral arm appendages.

1.3. Modeling

The work in this chapter capitalizes upon the unique properties of *Cassiopea* in order to examine the pulse-driven flow of water over the oral arms uncoupled from swimming. Since feeding and other types of particle exchange rely on fluid flow around the prominent oral arms, it is important to include the oral arms in examination of flow around the bell of *C. xamachana*. Computational studies allow exploration of how the bulk flows generated by *C. xamachana* vary with scale, pulse frequency, and characteristics of the oral arms within and beyond the normal biological range. For instance the flow structures can be predicted in the absence of the oral arms. This is useful for understanding how the oral arms can alter the bulk flow and affect rates of particle transfer between an organism and its surroundings.

In the second chapter a mathematical model of an idealized *C. xamachana* bell and oral arms is constructed and used in immersed boundary simulations to examine the

effects of bell motion and secondary structures on the bulk flow. This model differs from those of previous studies the oral arms as a separate and prominent structure of the organism. The flow fields generated by the model are validated with experimental measurements of flow fields generated by laboratory specimens.

In the third chapter the model is extended to examine how the feeding currents generated by *C. xamachana* change in the presence of a slow current. Is the fluid motion generated by *C. xamachana* strong enough to influence the flow in a typical ambient current? A simplified model of a jellyfish in channel flow suggests how the motion of the organism influences the ambient flow. The channel is modeled as low velocity Pouiseuille (parabolic) flow. By varying the maximum mid-channel velocity the effect of the channel flow on flow rates across a jellyfish with and without oral arms can be predicted.

The fourth chapter includes a computational study of the interaction between neighboring jellyfish and considers a more complex model of the pulsing dynamics based on video recordings of real organisms. *Cassiopea* have been observed to be solitary as well as in close proximity to one another [**29, 57, 72, 38**]. Based on laboratory data and videos of *in situ* footage, the pattern of pulsing of jellyfish bells vary greatly over time. The contraction and relaxation times are regulated by muscle mechanics and the viscoelastic properties of the bell and are relatively invariant, but the length of time between contractions varies considerably. Experimental data presented here indicates a bimodal Gaussian distribution of the time between the expansion of the bell and its subsequent contraction. For the computational experiments, two models are placed side by side in a simulated tank. The proximity of the jellyfish is varied along with the pulse patterns and size of the jellyfish. Varying pulse timing patterns are generated using a discrete

time Markov process. The choice of a Markov process type model is motivated by the bimodal distribution of pause times and the appearance of a strong dependence on the current pause length on the length of the next pause in organisms. Quantitative values of the flow near the outside edges of the jellyfish as well as the flow between the jellyfish and across the region where the porous layer is present are calculated and compared to one another.

1.4. Immersed boundary method

The computational studies are implemented using the immersed boundary (IB) method. The IB method was originally developed by Peskin in the 1970s to simulate blood flow through the human heart [**62**]. Since its construction, the immersed boundary method and others inspired by it have gained popularity as computational solutions to fluid-structure interactions problems at low to moderate Reynolds numbers (Re) [**54**]. The Reynolds number is the dimensionless scaling parameter that reflects the ratio of the effect of inertial forces in a flow to the effect of viscous forces defined as $Re = \rho LU/\mu$, where ρ is the density of the fluid, L is a characteristic length of the system, U is a characteristic velocity of the system, and μ is the viscosity of the fluid. The IB method has been used to simulate biological systems and materials including, but not limited to, swimming organisms, insect flight, platelet aggregation, cell motility, biofilms, foams, and parachuting [**23, 30, 40, 53, 73, 76**]. For details on the derivation of the immersed boundary method see Peskin [**62**].

The IB method involves the definition of the fluid and the structure in separate frames. A viscous, incompressible fluid is discretized at node points on a fixed Cartesian grid (the Eulerian frame) with appropriate boundary conditions. The structure is

defined as an immersed boundary and is discretized in a moving Lagrangian framework with reference to the Cartesian grid, but independent of the node points. Defined this way, the discretization of the fluid grid can be relatively coarse while still allowing for complex geometries of the structure. Since the fluid grid does need not be redefined as the boundary moves through it, computational times for simulations are greatly reduced. The governing equations for the fluid are the two-dimensional Navier-Stokes (NS) equations for viscous, incompressible fluid given by

$$\rho\left[\frac{\partial \mathbf{u}(\mathbf{x},t)}{\partial t}+\mathbf{u}(\mathbf{x},t)\cdot\nabla\mathbf{u}(\mathbf{x},t)\right]=-\nabla p(\mathbf{x},t)+\mu\nabla^2\mathbf{u}(\mathbf{x},t)+\mathbf{f}(\mathbf{x},t) \tag{1.1}$$

$$\nabla\cdot\mathbf{u}(\mathbf{x},t)=0 \tag{1.2}$$

where ρ is the fluid density, $p(\mathbf{x},t)$ is the fluid pressure, μ is the dynamic viscosity of the fluid, $\mathbf{u}(\mathbf{x},t)$ is the fluid velocity, $\mathbf{f}(\mathbf{x},t)$ is the force per unit area acting on the fluid, $\mathbf{x}$ is the position of the fluid node point, and t is the time. Note that Equation (1.1) is the momentum equation and Equation (1.2) gives the incompressibility condition.

To approximate the force that the boundary applies to the fluid, moving tether points may be employed. This method is commonly used when a desired configuration or preferred mode of active force must be enforced [**56, 76, 77**]. Here the preferred configuration $\mathbf{Y}(s,t)$ will be defined by the position of the constructed mathematical model of the bell at time t and position s. The boundary is tethered to the preferred configuration by a set of elastic springs. The stiffness of the springs, k, is chosen so that as the preferred boundary is stepped through time, a force required to move the actual boundary close to the preferred position is generated. Thus the structural equation in the Lagrangian

framework is the simple Hookean relation assuming zero rest-length springs given by

$$\mathbf{F}\left(\mathbf{X}\left(s,t\right),t\right)=k\left(\mathbf{X}\left(s,t\right)-\mathbf{Y}\left(s,t\right)\right) \tag{1.3}$$

where $\mathbf{F}\left(s,t\right)$ is the force per unit length acting on the fluid, $\mathbf{X}\left(s,t\right)$ gives the Cartesian coordinates of the boundary. Here the forces acting on the boundary are assumed to be elastic forces based on Hookean springs, although more complicated rules and relations can also be included. The spring force in Equation (1.3) may be thought of as a singular force density defined along the immersed boundary.

The equations defined in the Lagrangian framework (1.3) and in the Eulerian framework (1.1,1.2) are coupled through the following fluid-structure interaction equations:

$$\mathbf{f}\left(\mathbf{x},t\right)=\int\mathbf{F}\left(\mathbf{X}\left(s,t\right),t\right)\delta\left(\mathbf{x}-\mathbf{X}\left(s,t\right)\right)ds \tag{1.4}$$

$$\frac{\partial\mathbf{X}}{\partial t}=\mathbf{U}\left(\mathbf{X}\left(s,t\right)\right)=\int\mathbf{u}\left(\mathbf{x},t\right)\delta\left(\mathbf{x}-\mathbf{X}\left(s,t\right)\right)d\mathbf{x} \tag{1.5}$$

where ds is the arclength along the boundary, and $\mathbf{U}\left(s,t\right)$ is the local fluid velocity at the boundary point s. Equation (1.4) communicates the force exerted by the boundary on the fluid grid using a smoothed two-dimensional Dirac delta function $\delta\left(\mathbf{x}\right)$. The choice of the 2-D δ-function used here is given by

$$\delta_{h}\left(\mathbf{x}\right)=\frac{1}{h^{2}}\phi\left(\frac{x}{h}\right)\phi\left(\frac{y}{h}\right) \tag{1.6}$$

where

$$\phi(r) = \begin{cases} \frac{1}{4}\left(1 + \cos\left(\frac{\pi r}{2}\right)\right) & |r| \leq 2 \\ 0 & \text{otherwise} \end{cases} \tag{1.7}$$

and is detailed in [**64**]. The force that is now defined in the Eulerian framework is added to the NS equations through the force term $\mathbf{f}(\mathbf{x}, t)$ in Equation (1.1). The NS equations are solved using a fluid solver appropriate for the fluid domain and boundary conditions. For each of the projects described here, the underlying fluid domain is a square $N \times N$ periodic domain, so that a Fast-Fourier Transform-based fluid solver is appropriate. Once the NS Equations have updated the fluid information for the time step, Equation (1.5) is used to interpolate the local fluid velocity at each boundary point and move the boundary at the calculated velocity. This enforces the no-slip condition associated with a viscous fluid.

The basic steps of the IB method may be summarized as:

(1) A force is imposed on the immersed boundary.

(2) The force is translated to the fluid grid using a smoothed approximation to the Dirac δ-function.

(3) The fluid equations are solved using an appropriate numerical solver.

(4) The boundary is moved at the local fluid velocity which is found through interpolation using the smoothed δ-function to enforce the no-slip condition.

(5) The simulation advances to the next time step.

At the beginning of each time step, the above list is initiated and performed to update the fluid velocity and pressure as well as the position of the immersed boundary. The

procedure is continued at each time step until the final time is reach. The final time is prescribed so that the organism models complete the desired number of pulses. See Appendix A for more details on the discretization and implementation of the immersed boundary method used in this dissertation.

CHAPTER 2

Fluid Flow around the Bell of the Upside-Down Jellyfish

Cassiopea xamachana

2.1. Introduction

A two-dimensional (2D) model of *C. xamachana* was developed in order to examine the flow of fluid around the organism. The model was adapted from previous models of jellyfish to simulate *C. xamachana* [**17, 20, 15**]. In previous work, the cross-sectional shape of the bell was modeled as a time-varying hemi-ellipsoid. Here the shape was modified to more closely match that of *C. xamachana*. In addition a porous layer was added to represent the region of the oral arms. The timing of the bell pulses was determined using video recordings of laboratory specimens. The model was used to drive the boundaries in the immersed boundary method, generating the forces necessary for the preferred motion of the bell.

Exploration of a wide parameter space was used to test the physical limits of transport mechanisms and to identify cooperative or complementary feeding and exchange mechanisms. In this chapter, the contraction kinematics, the presence and porosity of the oral arms, and dynamic scaling were varied across and beyond the normal range of biologically relevant parameters. Net flow rates around the bell were calculated to examine fluid movement associated with the feeding mechanisms and the effect of changing parameters on bulk flow properties.

2.2. Materials and Methods

2.2.1. Measurements. Specimens of *C. xamachana* were obtained from Carolina Biological Supply Company (Burlington, NC) and Gulf Specimen Marine Laboratories, Inc. (Panacea, FL) and maintained in the laboratory in standard 29-gallon aquaria. Video recordings of the organisms were obtained using a Panasonic Palmcorder (Model No. PV-GS300, 29.97 fps.) The timing of the pulse cycle was analyzed for 410 seconds of

movement using iMovie software by Apple, Inc. to obtain a realistic cycle pattern. The contraction of the bell was defined as the time during which the bell moved toward the central axis. The first pause was defined as the time during which the bell appears motionless before beginning its expansion. The expansion was defined as the motion of the bell out from the central axis of the organism. Finally the second pause was defined as the time that the bell appears motionless before the next contraction begins. See Figure 2.1 for examples of individual fields from the recordings. This pattern of motion was used as an input for the mathematical model of the organism.

The times determined from the video recordings were 0.6 ± 0.17 s for expansion,

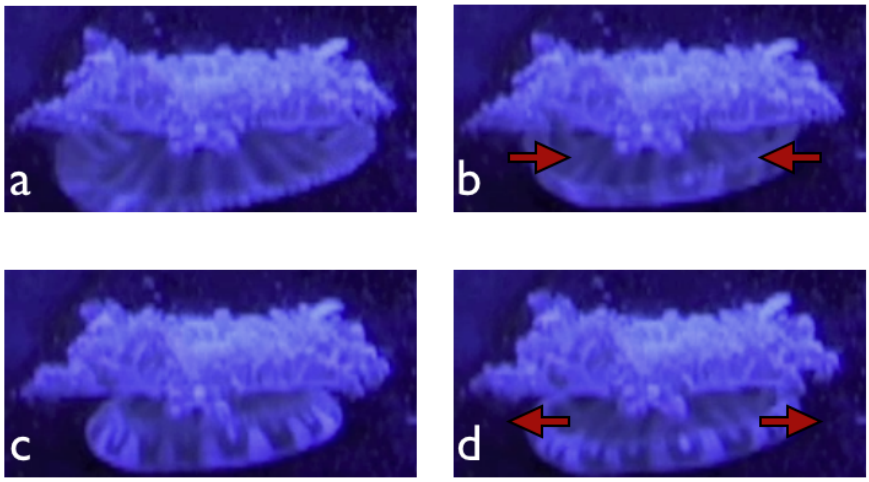

FIGURE 2.1. A time series showing the pulse of a *C. xamachana* bell. Left to right, top to bottom: a)The bell in a relaxed state. b)During contraction the bell moves up and toward the center of the organism. c)Once fully contracted the bell pauses slightly. d)The edges of the bell then begin to move down and away from the center of the organism. a)The relaxed bell pauses before the next contraction.

0.13 ± 0.06 s for the first pause, 0.7 ± 0.13 s for expansion, and 2.0 ± 1.30 s for the second pause with a sample size of 150 cycles from a single organism. The behavior of the organism was variable. These parameters were used as biologically reasonable but in no way a comprehensive description of the motion of the organism.

2.2.2. Construction of the model. An approximate model of the primary bell shape was developed for use as an input into the simulations. Extending previous models [**17, 47, 86, 66**] that describe jellyfish using hemiellipsoids or functions fit to digitized bell shapes, a simple mathematical model was constructed that captures the fundamental features of the organism. The models also included a representation of the oral arms as a separate structure. This addition is novel since previous studies typically ignore the oral arms since the focus organisms in these studies have reduced oral arms structures.

A simplified two-dimensional model of the bell of *C. xamachana* was constructed to make multiple parameter sweeps feasible. The aboral region resting against the substrate was defined as a line of length L. The choice of a line was justified by the fact that there is no flow under the aboral side of the jellyfish bell and in fact this area of the jellyfish is often lightly attached to the seafloor by suction[**5**]. This attached portion only slightly dilated during pulsation so this section was assumed to be of constant length throughout the motion. Two reference configurations were defined as a completely contracted state and a completely expanded state. The curve of each of these configurations was defined by Equation (2.1)

$$(x, y)(\theta) = \left(\frac{L}{A}\right)\left(\cos\left(\frac{\pi}{B}\right) + 2\pi\theta, C\sin\left(\frac{\pi}{B}\right) + 2\pi\theta\right) \tag{2.1}$$

where $A = 16$, $B = 2$, and $C = 1$ for the expanded sides of the bell and $A = 4$, $B = -1$, $C = 2$, and θ is equal to the angle between the major axis of the ellipse parallel to the Cartesian y-axis and the line drawn from the center of the ellipse to the corresponding point on the boundary for the contracted sides of the bell. A, B, and C were chosen such that the conformations have relatively simple geometries while also

giving a reasonable approximation of the morphology of the organism. To determine intermediate conformations between fully expanded and fully contracted configurations, the position was linearly interpolated using the calculated motion times from the video recordings. To interpolate, Equation 2.1 becomes

$$(x,y)(\theta) = \left(\frac{L}{A(t)}\right)\left(\cos\left(\frac{\pi}{B(t)}\right) + 2\pi\theta, C(t)\sin\left(\frac{\pi}{B(t)}\right) + 2\pi\theta\right) \tag{2.2}$$

where $A(t), B(t)$, and $C(t)$ change in time in order to contract and expand the bell margins. Let the contraction start at $t = 0$. Let the time t_1 be the time when the first contraction ends, t_2 the time when the first pause ends, t_3 the time when the relaxation ends, and t_4 the time when the second pause ends. $A(t), B(t)$, and $C(t)$ were then given as

(2.3)

$$\begin{array}{llll}
A(t) = 16 - 12\left(\frac{t}{t_1}\right) & B(t) = 2 - 3\left(\frac{t}{t_1}\right) & C(t) = 1 + \left(\frac{t}{t_1}\right) & 0 \le t < t_1 \\
A(t) = 4 & B(t) = -1 & C(t) = 2 & t_1 \le t < t_2 \\
A(t) = 4 + 12\left(\frac{t-t_2}{t_3-t_2}\right) & B(t) = -1 + 3\left(\frac{t-t_2}{t_3-t_2}\right) & C(t) = 2 - \left(\frac{t-t_2}{t_3-t_2}\right) & t_2 \le t < t_3 \\
A(t) = 16 & B(t) = 2 & C(t) = 1 & t_3 \le t \le t_4
\end{array}$$

Recall the Reynolds number (Re) is the dimensionless scaling parameter that reflects the ratio of the effect of inertial forces in a flow to the effect of viscous forces. For $Re \ll 1$, viscous forces are dominant in the system. For$Re \gg 1$, inertial forces are significant while viscous forces are often negligible. Here Re was defined using the Equation $Re = \rho LU/\mu$, where ρ was the density of the fluid, L was the length of the aboral region of the bell, U was the average velocity of the tip of the bell during contraction, and μ was the viscosity

of the fluid. The Re for adult *C. xamachana* is generally in the hundreds. In this chapter the parameters were computationally explored at Re 450, which was within the normal range of the adult organism. Also considered were parameters at Re 45, appropriate for the juvenile ephyra that do not remain on the ocean floor. This parameter choice was included to examine the size limits of pulse-driven fluid transport.

The effect of pauses between pulses (the so-defined second pause) on the resulting fluid motion were also explored. From the analysis of video recordings, the organism exhibit two types of pauses. The representative organism displayed a second pause between 1.0-3.5 seconds, while the remainder of the time a slight delay between $0.13 - 0.4s$ was observed. It is important to note that there was noticeable variation in the pulsing frequencies of *C. xamachana* and other jellyfish [**11**], and the values used here were selected from a representative organism. The nature of the pauses was explored in more detail in Chapter 4. In the numerical simulations of the current chapter, the pause time was varied to test the effect of the length of the pause on the bulk flow around the bell. The computational model thus allowed one parameter to be varied in a controlled and specified manner.

To examine the effect of the oral arms on the bulk flow, a simple model of the oral arms was constructed as a porous barrier placed just above the top of the bell (Figure 2.2.) This model was used to provide an obstruction to flow while still allowing some fluid transport through the layer. The flow through the elaborate oral arms is obviously more complex, but modeling it represents a challenging multiscale problem. It is currently not feasible to accurately capture both the large-scale flow patterns generated by the bell while also resolving the fine details of the flow through the branches of the oral arms. Some of the

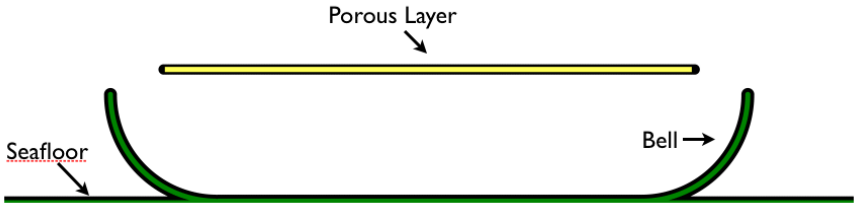

FIGURE 2.2. A diagram showing the jellyfish model. The porous layer is shown in yellow. The seafloor and main part of the jellyfish bell are shown in green and black.

challenges of even relatively simple fluid-structure interaction problems were discussed in [**7**] and [**35**]. The model presented here represents a first step in understanding the effect of the oral arms on the bulk flow generated by the jellyfish. The porosity of the oral arm model allows water to flow through this layer, and this was one of the most obvious features that should be included in this study on fluid transport. For a first approximation of porosity, a homogeneous material was assumed. The computational methods used to describe the porous layer are given below.

The complex structure of the eight oral arms was modeled as a porous layer using the method derived by [**41, 73**]. Permeability was incorporated into the immersed boundary method using Darcy's law which states that the relative velocity of a fluid through a porous medium is proportional to the pressure difference across the boundary:

$$q = \frac{-\kappa}{\mu}\,[P] \tag{2.4}$$

where q is the Darcy flux (discharge per unit area), κ is the permeability of the layer, and $[P]$ is the pressure drop across the layer.

Equating the flux to the difference between the local fluid velocity and the boundary

velocity results in an expression for the slip between the boundary and fluid that is proportional to the permeability and the pressure drop. This was incorporated into the immersed boundary method by modifying the velocity of the boundary. Rather than moving the boundary at the local fluid velocity, a slip was used that was proportional to the force per unit area acting normal to the boundary (which is equivalent to the pressure drop) and the porosity. Equation (6) was modified as follows:

$$\frac{\partial \mathbf{X}}{\partial t} = \mathbf{U}(s,t) + \lambda \left(\mathbf{F}(s,t) \cdot \mathbf{n}\right) \mathbf{n} \tag{2.5}$$

where λ was a proportionality constant termed the porosity by Kim and Peskin [**41**]. Note that this was equivalent to reducing the drag force applied to the fluid by the boundary. The physical interpretation of the porosity coefficient, λ, is that it is equal to the number of pores in an interval multiplied by the conductance of the material per unit arc length. The relationship between the porosity, λ, and the permeability, κ, was given by $\lambda = \kappa / (A\mu)$, where A was the area of the porous material. Kim and Peskin (2006) used the porosity coefficient in the slip term while Stockie (2009) used the permeability, a value that can be readily found in the literature for a variety of materials. The effective porosity or permeability of jellyfish oral arms are not known. For these simulations several orders of magnitude of values for the porosity were considered. For the remaining simulations a value was selected that produced flow profiles similar to those observed experimentally. This value was chosen so that there was substantial flow through the porous layer but the layer clearly altered the resulting flow patterns.

To model the oral arms in the simulations that follow, a line was defined of length L (the same length as the aboral region of the bell) as a reasonable approximation of length

based on qualitative observations. The line was positioned just above the opening of the bell and was tethered in place using stiff Hookean springs that resisted deformations in this part of the boundary. As a first approximation, the oral arms model was held in place and maintained a constant porosity.

Simulations were performed on a 512×512 periodic grid. The size of the domain was $4L \times 4L$ the length of the jellyfish body. A box connected to tether points and stiff springs was added $L/8$ inside the edges of the domain to simulate the conditions in the laboratory tanks used for dPIV. The parameters used in the numerical simulation are given in Tables 2.1 and 2.2 Times for the contraction, pauses, and relaxation were

TABLE 2.1. Values of all parameters in the simulations unless otherwise noted

Parameter	Value
Density $[\rho]$ (kg/m3)	998
Body Length $[L]$ (m)	0.0508
Porosity coefficient $[\lambda]$ $(m^2/(N \cdot s))$	0.0000072
Cycle period $[t_1 + t_3 - t_2]$ (s)	1.3
Duty cycle $[t_1/t_4]$	0.4615
1st pause $[t_2 - t_1]$ (s)	0.13
2nd pause $[t_4 - t_3]$ (s)	2.0
Total period $[t_4]$	3.43

TABLE 2.2. Default values of all parameters in the simulations unless otherwise noted

Numerical Parameter	Value
timestep $[dt]$ (s)	0.00006096
Cartesian grid spatial step $[h]$ (m)	0.000396875
Lagrangian spatial step $[ds]$	0.000198438
Domain size (m)	0.2032
Stiffness coefficient, bell and box $[k]$ (N/m)	13987028
Stiffness coefficient, porous layer $[k_p]$ (N/m)	139870.28
Fluid grid size	512 x 512

taken from video recordings as described previously. The mathematical model without the addition of the oral arms structure was referred to as the bell-only model. The

models incorporating a porous layer and an impermeable layer will be referred to as the porous model and the impermeable model, respectively. *Re* was varied by changing the dynamic viscosity of the system. This method of changing *Re* has been used previously as an efficient means of exploring a large parameter space without requiring changes in multiple parameters (velocities, length scales) [**4, 81**].

2.3. Results

2.3.1. Changes in Reynolds number. Vorticity plots with velocity vectors are shown for $Re = 45$ and $Re = 450$ in Figure 2.3. Frames a-d show $Re = 45$ and frames e-h show

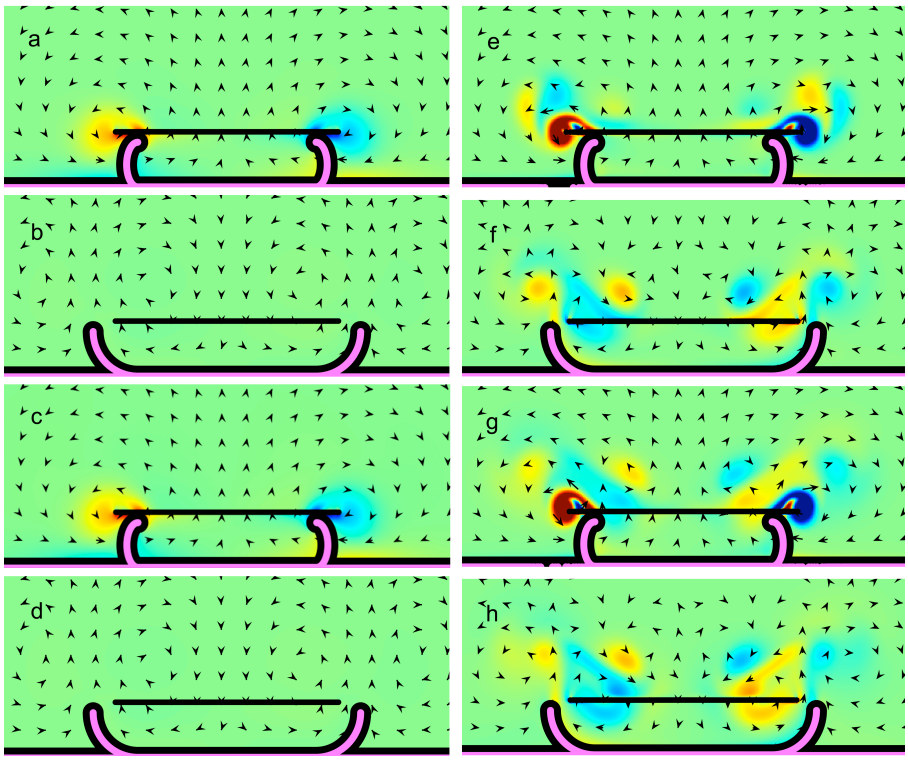

FIGURE 2.3. Vorticity plots from numerical simulations with overlain velocity vector fields. Warm colors show regions of positive vorticity while cool colors are areas of negative vorticity. Panels (a) through (d) show vorticity plots for the porous model at *Re* 45 after (a) the second contraction, (b) the second full cycle, (c) the fourth contraction, and (d) the fourth full cycle. Panels (e) through (h) show corresponding plots at *Re* 450.

$Re = 450$. Snapshots were taken during the second pulse cycle at the end of contraction

(a,e) and at the end of expansion (b,f). Snapshots are also shown during the fourth cycle at the end of contraction (c,g) and at the end of expansion (d,h). Warm colors represented regions of positive vorticity and cool colors represent regions of negative vorticity. The target boundary (purple) and the actual boundary (black) remain indistinguishable to the naked eye. For $Re = 45$, starting vortices formed at the tip of the bell margin during the beginning of contraction, and oppositely signed stopping vortices formed at the beginning of expansion. At the end of each phase vorticity quickly dissipates, and the vortices did not appear to separate from the tip of the bell. For $Re = 450$ starting and stopping vortices formed at the beginning of contraction and expansion, respectively. In contrast to the low Re case the vortices did separate from the tips of the bell margins and were advected with the fluid along the porous layer. The fluid along the floor was pulled towards the bell on average during the cycle.

To quantify the bulk flow near and across the bell in the simulations the volumetric flow rate through a region was calculated. To calculate the VFR a 'flow' line was drawn in a region so that the line was normal to the flow in the direction of interest (Figure 2.4.) The instantaneous velocity in the normal direction was integrated along the flow line and was normalized against the length of the line to obtain the volume flux per unit length as

$$\frac{V}{l} = \int_S \mathbf{u} \cdot \mathbf{n} dS \tag{2.1}$$

where S was the flow line, $\mathbf{u}$ was the velocity along the line, $\mathbf{n}$ was the unit vector normal to the flow line, V was the volume flux, and l was the length of the flow line. In this chapter, two flow lines were defined. The first flow line was drawn vertically near the

bottom of the tank to give a measurement of horizontal flow toward the bell (Figure 2.4). This flow line was referred to as the horizontal flow line (HFL), and its length was set

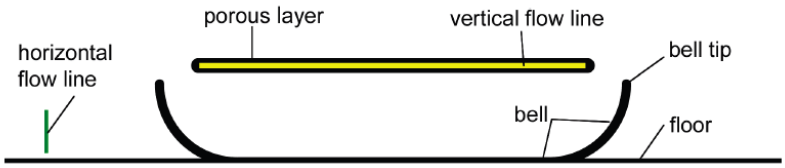

FIGURE 2.4. The fully expanded model of the bell with the oral arms modeled as a porous line. The substrate has been added to the model as a straight line one spatial gridpoint away from the model. The green line shows the positioning of the horizontal flow line (HFL) and the yellow line shows the position of the vertical flow line (VFL) where volume fluxes are calculated.

equal to the height of the bell at a distance $0.4L$ away from the outer edge of the relaxed bell. The second line, the vertical flow line (VFL), was drawn horizontally and overlaid on the center of the porous structure. The VFL's length was set to be $L - 3 * ds$. where ds was the spatial step size on the Lagrangian grid, to ensure the flow line was in the region of the porous structure throughout the simulations.Typically ds was set to $\frac{1}{2}$ of the spatial step size on the Cartesian grid, h.

The flow rate along the HFL (HFR) was normalized by dividing by the length of the HFL. Positive values of the HFR always corresponded to flow toward the bell while negative values corresponded to flow away from the bell on both sides of the model. In the case of the vertical flow line (VFL), the flow rate across the line (VFR) was normalized by dividing by the length of the VFL. Positive values corresponded to flow away from the bell while negative values corresponded to flow toward the bell. For the HFRs the large increase in flow toward the bell corresponded to the beginning of the bell contraction.

The decrease in the flow toward the bell occurred during the first pause and the expansion phase. During the second pause (if it was present), the flow toward the bell slowed and in some cases reversed. For the longer pauses a gradual increase in flow toward the bell and a plateauing of the flow rate was observed before the next contraction began. For the VFRs, a similar pattern was observed for flow away from and toward the porous layer. Examples of the general pattern of flow rates corresponding to each phase of the pulse cycle are given in Figure 2.5.

The HFR at $Re = 45$ and $Re = 450$ for models both with and without the porous

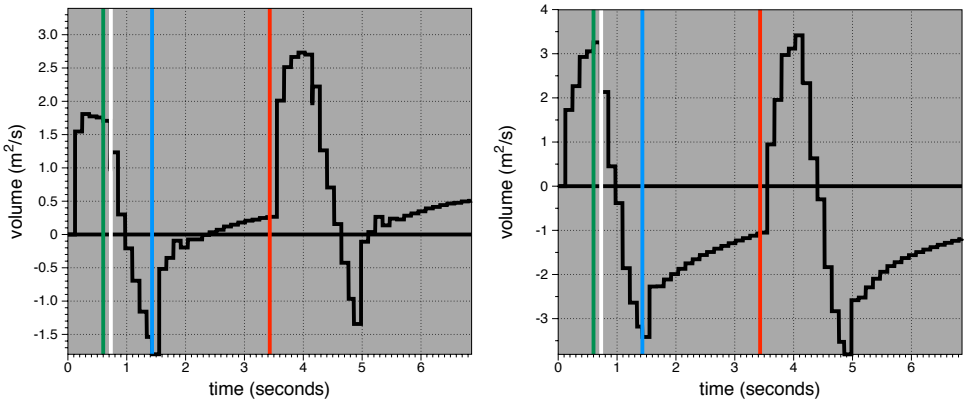

FIGURE 2.5. A diagram of the pattern of the model organism's pulse cycle for the HFR(left) and VFR(right). The cycle starts at the beginning of the domain at $t = 0$ s. The region between the beginning of the diagram and green line corresponded to the contraction of the model. The region between the green and white lines corresponded to the short pause between contracting and relaxing. The region between the white line and the blue line corresponded to the relaxation of the bell. The region between the blue line and the red line corresponded to the second longer pause at the end of the cycle.

structures are shown in Figure 2.6 over four contraction cycles. Positive flow rates represent fluid motion towards the bell. For each simulation, the maximum HFR occurred during the contraction period of the cycle. During bell expansion, the HFR quickly decreased and became negative (flow moves away from the bell). After the end of the bell expansion, the HFR quickly approached zero. The minimum HFR (greatest flow rate

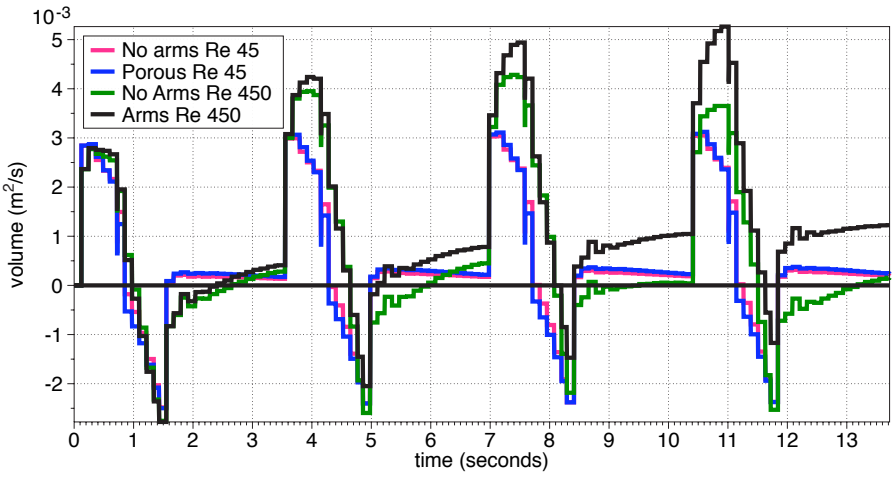

FIGURE 2.6. Volumetric flow rates along the HFL describing horizontal flow moving towards the bell are compared among simulations of four different models. The bell-only model at Re 45 is shown in pink, almost completely overlapped by the porous model (blue). A bell-only model (green) and a porous model (black) are also shown. These plots indicate the normalized horizontal flow from the left of the domain toward the model organism. Positive flow indicates fluid moving toward the structure, while negative flow indicates flow moving away from the structure.

away from the bell) decreased after each pulse in the $Re = 450$ simulations with the added porous layer. In the other cases, substantial amounts of backflow away from the bell during expansion persisted for all cycles. The VFR is shown in Figure 2.7. The maxima and minima of the flow rates occur during the contraction and expansion, respectively. The magnitude of the VFR quickly dropped to zero for $Re = 45$ when the jellyfish is at rest. For $Re = 450$ the more substantial flow persisted through the porous layer during relaxation.

2.3.2. The effect of porosity. The effect of the oral arms on the flow was examined by comparing the bell-only model to a model incorporating a permeable structure as well as to a model incorporating an impermeable structure. Representative vorticity plots with velocity vectors of the impermeable layer are shown in Figure 2.8 during the second cycle (a,b) and the fourth cycle (c,d). Note that the way in which the starting and

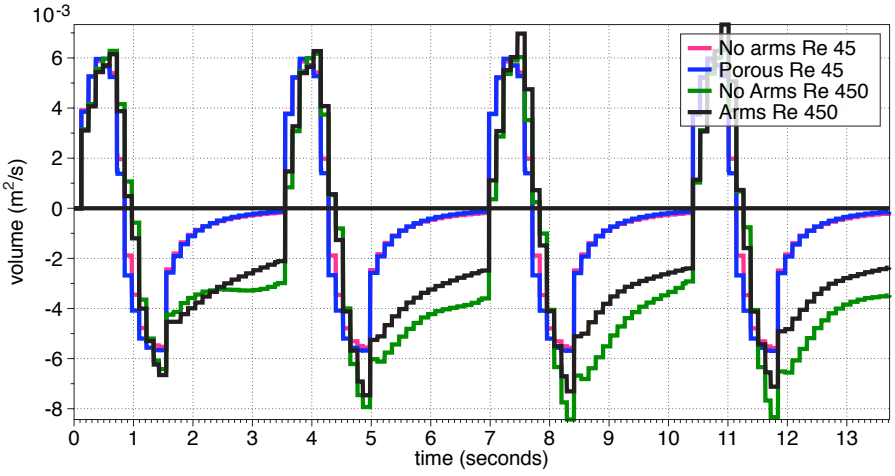

FIGURE 2.7. Volumetric flow rates along the VFL describing vertical flow moving through the porous layer region are compared among simulations of four different models. The bell-only model at Re 45 is shown in pink, almost completely overlapped by the porous model (blue). A bell-only model (green) and a porous model (black) are also shown. These plots indicate the normalized vertical flow from through the region where the porous structure (if present) is defined. Positive flow indicates fluid moving up away from the structure, while negative flow indicates flow moving down into the cavity of the structure.

stopping vortices were advected in the fluid was dramatically altered by the layer. In the case of the porous layer in Figure 2.3(e-h), the vortices swirl around the outer edges of the simplified oral arms. For the case of the impermeable layer, a pair of oppositely spinning vortices was formed at each bell margin during the initial stages of contraction (in contrast to the formation of one starting vortex formed at each bell margin). This pair of vortices was quickly advected away from the bell. During expansion, another pair of oppositely signed vortices formed at each bell margin that remains trapped between the bell and oral arms. In the absence of the oral arm layer (not shown in figures), starting and stopping vortices formed during each cycle and swirl around the bell margins.

Plots of the HFRs vs. time for a porous layer model, an impermeable layer model and the bell-only model at $Re = 450$ are shown in Figure 2.9. The maximum flow was achieved during the contraction for the bell-only model and the porous model, while

the maximum HFR for the impermeable model occurred during the contraction in some pulses and the relaxation during others. The minimum HFR for the impermeable model decreased after each successive pulse cycle. The VFR is shown in Figure 2.10. The impermeable model showed much less flow than the porous and the bell-only models, and the flow that was present was due to small deformations of the layer. The porous model and the bell-only model showed similar flow patterns throughout all four pulse cycles.

Different values of the porosity parameter λ were compared for the porous model at $Re = 450$. Figure 2.11 shows the HFR. The HFR pattern was similar among them, but different in magnitude along the HFL throughout the pulse cycle. As the porosity of the porous layer increases, the maximum flow rate increases. As the porosity decreases, the flow rates approached the impermeable case as expected. The VFR is shown in Figure 2.12. The pattern of exchange was similar across the VFL for each value of the porosity with an increase in the maxima and minima similar to those of the HFR.

To test the choice of the porosity coefficient used in this in this chapter, λ was varied over 4 orders of magnitude. The VFRs describing vertical flow moving through the porous layers are shown in Figure 2.13. The dashed blue line denotes the value of the porosity chosen for the bell-only cases. Notice that when $\lambda = 7.2 \times 10^{-10}$ the VFR at the porous layer was similar to the case of the solid layer. For values of λ between 7.2×10^{-7} and 7.2×10^{-6} the difference in the volumetric flow rates was negligible despite the order of magnitude difference in λ. These results suggest that very small values of porosity would yield results similar to a solid layer while large values of the porosity would have little

effect on the flow. Intermediate values of λ altered the bulk flow while allowing some flow through the layer. The result was similar for a large range of intermediate λ.

2.3.3. The effect of pauses. Vorticity plots with velocity vectors of the flow generated by a contracting and expanding bell without pauses are shown in Figure 2.14. The vorticity during the second cycle is shown immediately after contraction (a) and immediately after expansion (b). The vorticity during the fourth cycle is also shown after contraction (c) and expansion (d). Continuous pulsing resulted in a train of vortices being advected vertically up and away from the model. In comparison, when pauses were included (Figure 2.3 e-h) the vortices moved around the porous layer and mostly dissipated before the next cycle.

The HFRs were compared for a porous model with different pause times between complete expansion and the next contraction as shown in Figure 2.15(a-c). The maximum and minimum HFRs occur during contraction and expansion, respectively. In general, the shorter the pause time the greater the magnitude and duration of backflow during expansion. A net flow towards the bell was also generated during the relaxation that decreased for pause times greater than 2 seconds.

2.3.4. Comparison of Simulations to DPIV data. The vorticity plots from the simulation with porous arms in Figure 2.3 were compared to data obtained using digital particle image velocimetry (PIV) in Figure 2.16 from Santhanakrishnan et al. (submitted). Particle image velocimetry was used to obtain instantaneous information on the flow field surrounding a live *C. xamachana* by recording and processing single or multiple exposed images of tracer particles suspended in the fluid. The particle images were then processed using correlation-based techniques to construct the velocity vector field of the

fluid flow [**1, 85**]. Figure 2.16 shows the velocity vector fields generated by the pulse cycle near the end of contraction (a) and near the end of expansion (b). Comparing Figure 2.16(a) to 2.3(g), the presence of a clear starting vortex was seen at the end of contraction with strong flow moving along the floor towards the bell. Flow fields at the end of expansion in Figure 2.16(b) and 2.3(h) show continued flow towards the bell, the strongest flow upward near the edge of the orals arms, as well as flow across the top of the oral arms. Both the bell-only model and the impermeable model did not exhibit this flow structure. This indicates that both the presence of an obstruction (such as the oral arms) and its porosity strongly influenced the dynamics of the bulk fluid flow.

The velocity fields to the left of the bell in both the PIV and the porous model show a constant flow toward the bell. Given the position of the HFL, a positive HFR represents net flow toward the bell in that region, while a negative value indicated flow away from the bell. In the PIV data, constant flow toward the bell from the area near the floor was seen in the vector field plots. In Figure 2.7, after the third pulse almost all of the flow along the substrate moves toward the bell. This was not the case in the bell-only model and the impermeable model simulations (see Figures 2.7 and 2.9), and these results suggest that the oral arms play a role in directing the flow toward the bell.

2.4. Discussion

The results presented here suggest that 1) feeding from flows driven by bell contractions in a benthic jellyfish may only be effective for Re on the order of 100 or higher, 2) the porous structure of the jellyfish oral arms substantially altered bulk flow properties around the organism, and 3) changes in the duration of the pause between bell contractions dramatically altered the resulting flow fields. Furthermore, the results suggest that

the role of secondary structures such as the oral arms should be taken into account when designing models of some organisms, particularly oblate jellyfish with prominent feeding structures. In many oblate jellyfish, the oral arms comprise a substantial portion of the body mass of the organism and often extend past the edges of the bell into the region of vortex formation [**8, 36**]. Previous models of jellyfish have focused on how flow was driven to these structures, but results here indicate that these structures may also alter the larger scale flow field. The results support the hypothesis that jellyfish use bell pulsations not only for locomotion but also to move water and food particles to the secondary mouths. *C. xamachana* in particular rely on the ability to drive fluid for sampling, but other jellyfish that slowly cruise may be capitalizing upon this mechanism to compensate for the high cost of locomotion.

For $Re = 45$ which was below the normal biologically relevant adult range, little net flow was brought to the oral arms via the bell pulsations (see Figure 2.7). A careful examination of the flow fields also indicates that little mixing occurred around the region of the oral arms. This suggests that there was a limit to the utility of pulsation as a particle transfer mechanism in the intermediate Re range. It is not surprising that juvenile *C. xamachana* do not and rest inverted on the ocean floor until they reach a bell diameter of about 2 cm or more [**8**]. Figure 2.3 shows that at higher Re fluid moves across the oral arms, indicating that the pulsatile motion promotes water sampling in this range. Added together, this suggests that the motion toward the bell and the increased sampling enhances the ability of the bell to bring draw in materials from the water adjacent to the substrate as well as the ability to sample the incoming fluid. Enhancement was not observed at lower Re.

Figures 2.9 and 2.10 indicate that the presence of an impermeable obstruction in the path of the flow not only prevents exchange across the secondary structure where feeding would occur, but it also directs flow from the substrate away from the bell, reducing the likelihood of particle sampling from the floor. A solid obstruction would thus be less useful in enhancing feeding through pulsation. The flow pattern in Figure 2.10 shows that without the secondary structure present, the fluid moved back and forth as it moves toward the bell. This suggests that the porous layer plays an important role in augmenting fluid flow to the bell.

Laboratory observations show that *C. xamachana* exhibit different pause durations between pulses. As shown in Figure 2.14(a), without a pause the flow does not move increasingly towards the bell with each cycle. This indicates a reduction in the amount of new fluid brought to the bell along the floor with each pulse. When the pause is included in the simulation, the flow immediately above the oral arms moves across the layer with net flow at the oral arms moving downwards and potentially bringing food to the secondary mouths. Both types of cycles were observed in *C. xamachana*, and these results suggest that slight modifications in the pulsing dynamics could significantly alter the resulting flow fields. For example, pauses might allow for the water that was brought into the bell to be sampled for a longer period of time. Pulsing cycles without pauses might be used for swimming and to move fluid up and away from the animal.

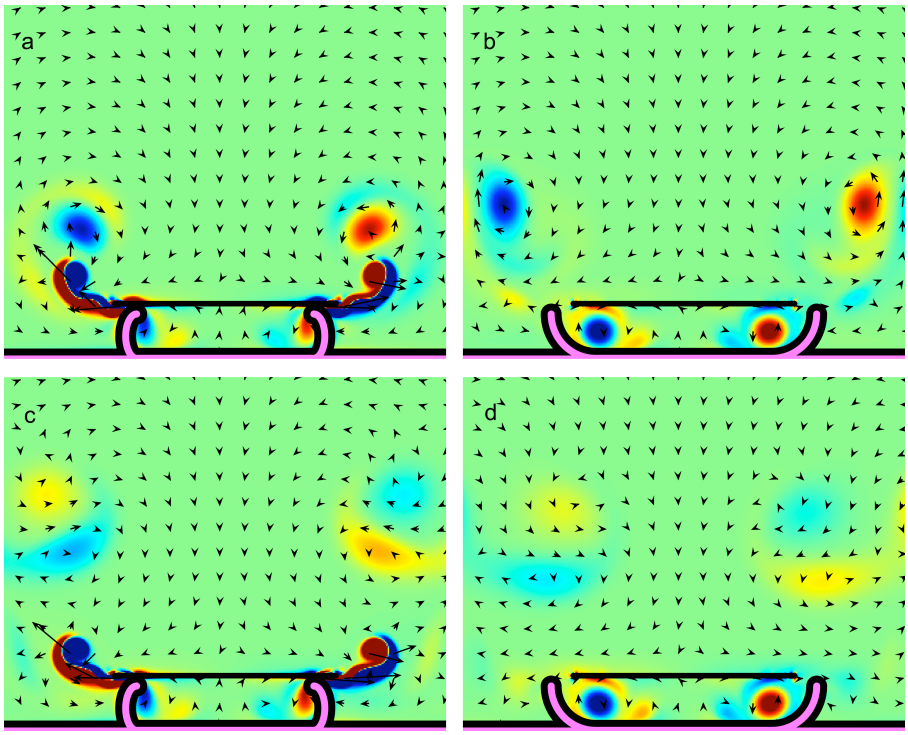

FIGURE 2.8. Vorticity plots for the impermeable model from numerical simulations with overlain velocity vectors. Warm colors show regions of positive vorticity while cool colors are areas of negative vorticity. Panels (a) through (d) show vorticity plots for the impermeable model at *Re* 450 after (a) the second contraction, (b) the second full cycle, (c) the fourth contraction, and (d) the fourth full cycle.

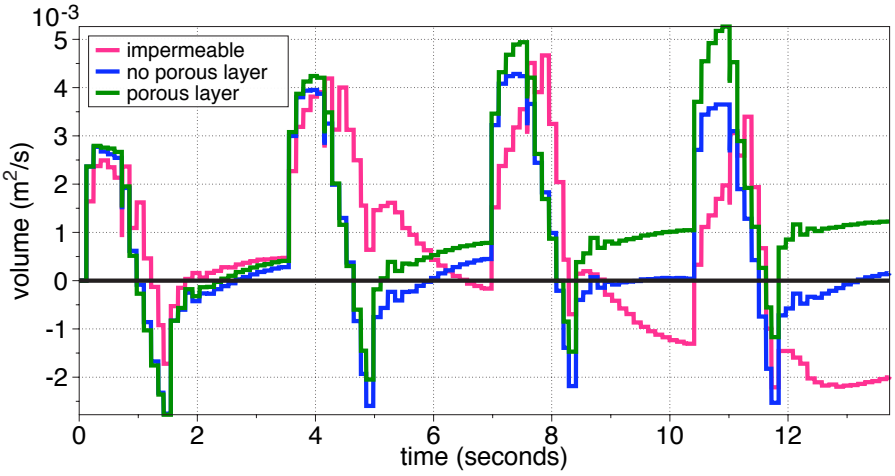

FIGURE 2.9. Volumetric flow rates along the HFL describing horizontal flow moving towards the bell were compared among simulations of three different models. The bell-only model at *Re* 450 is shown in blue. The porous model (green) and the impermeable model (pink) are also shown at the same Reynolds number. These plots indicate the normalized horizontal flow from the left of the domain toward the model organism. Positive flow indicates fluid moving toward the structure, while negative flow indicates flow moving away from the structure.

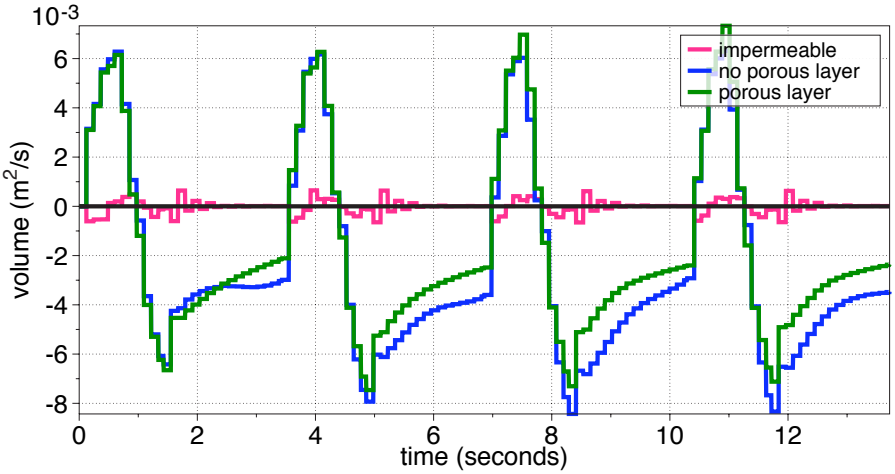

FIGURE 2.10. Volumetric flow rates along the VFL describing vertical flow moving through the porous layer (if present) were compared among simulations of three different models. The bell-only model at *Re* 450 is shown in blue. The porous model (green) and the impermeable model (pink) are also shown at the same Reynolds number. These plots indicate the normalized vertical flow from through the region where the porous structure (if present) is defined. Positive flow indicates fluid moving up away from the structure, while negative flow indicates flow moving down into the cavity of the structure.

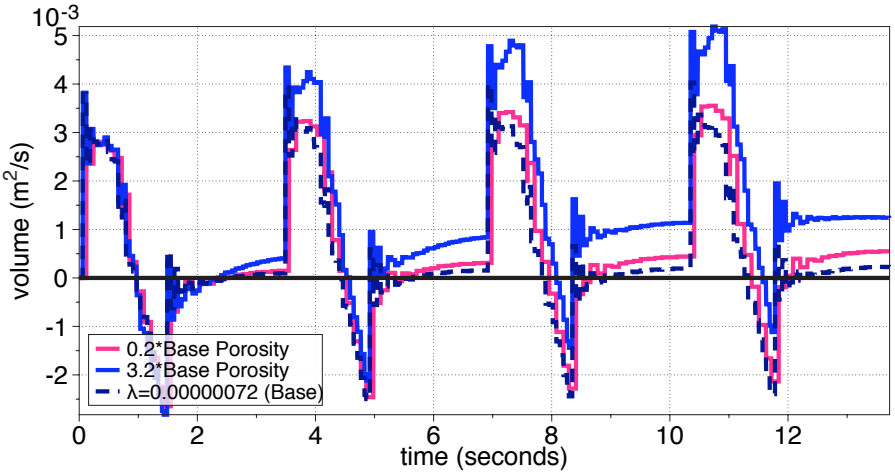

FIGURE 2.11. Volumetric flow rates along the HFL describing horizontal flow moving towards the bell were compared among simulations of three different models. The porous model at *Re* 450 is shown in black. Models with a porosity coefficient that is 20% of the porous model (pink) and with a porosity coefficient that is 320% of the porous model (blue) are also shown at the same Reynolds number. These plots indicate the normalized horizontal flow from the left of the domain toward the model organism. Positive flow indicates fluid moving toward the structure, while negative flow indicates flow moving away from the structure.

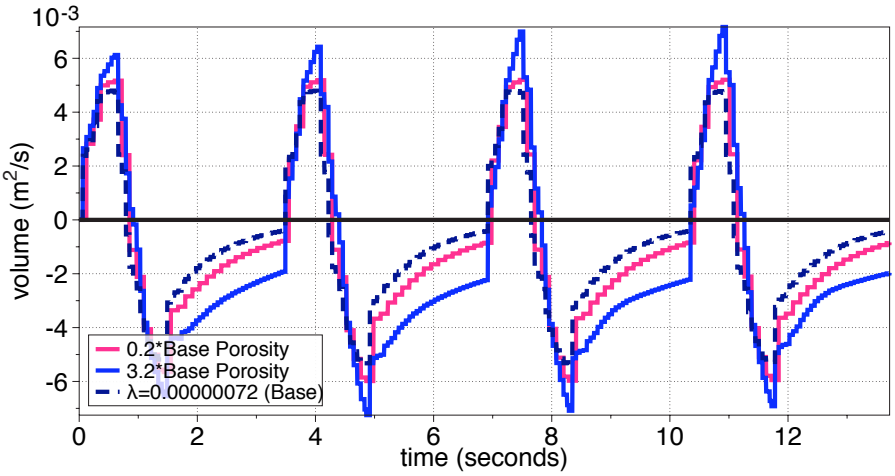

FIGURE 2.12. Volumetric flow rates along the VFL showing vertical flow through the porous layer were compared among simulations of three different models. The porous model at *Re* 450 is shown in black. Models with a porosity coefficient that is 20% of the porous model (pink) and with a porosity coefficient that is 320% of the porous model (blue) are also shown at the same Reynolds number. These plots indicate the normalized vertical flow from through the region where the porous structure (if present) is defined. Positive flow indicates fluid moving up away from the structure, while negative flow indicates flow moving down into the cavity of the structure.

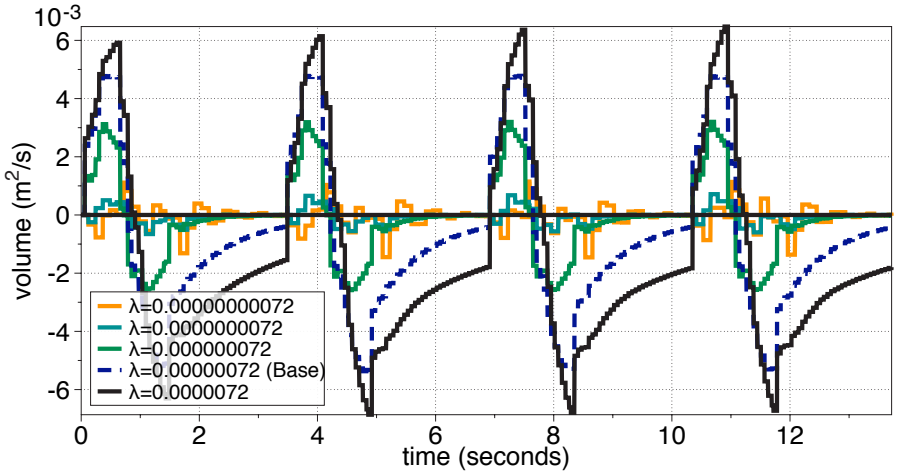

FIGURE 2.13. Volumetric flow rates along the VFL describing vertical flow moving through the porous layer for values of the porosity, λ, ranging over 4 orders of magnitude. The dashed blue line denotes the value of the porosity chosen for the bell-only cases. Notices that when $\lambda = 7.2 \times 10^{-10}$ that the volumetric flow rate at the porous layer was similar to the case of the solid layer. For values of λ between 7.2×10^{-7} and 7.2×10^{-6} the volumetric flow rates at the layer were very similar.

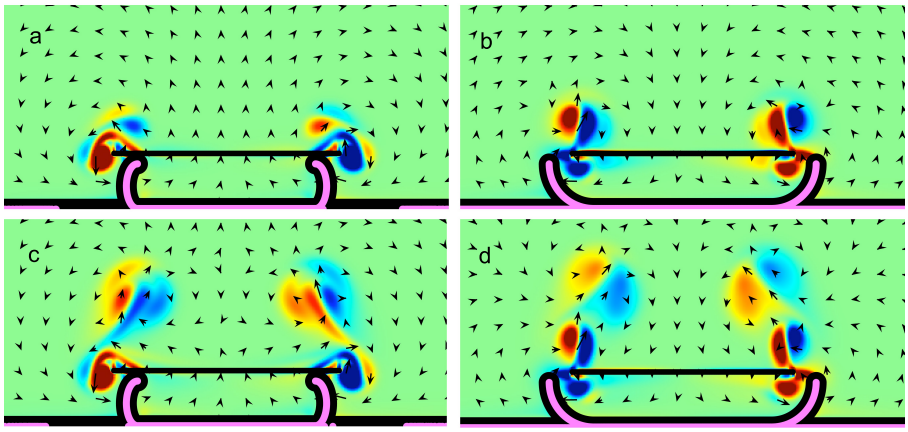

FIGURE 2.14. Vorticity plots from numerical simulations with overlain velocity vector fields for the porous model without a pause. Warm colors show regions of positive vorticity while cool colors are areas of negative vorticity. Vorticity fields are after (a) the second contraction, (b) the second full cycle, (c) the fourth contraction, and (d) the fourth full cycle.

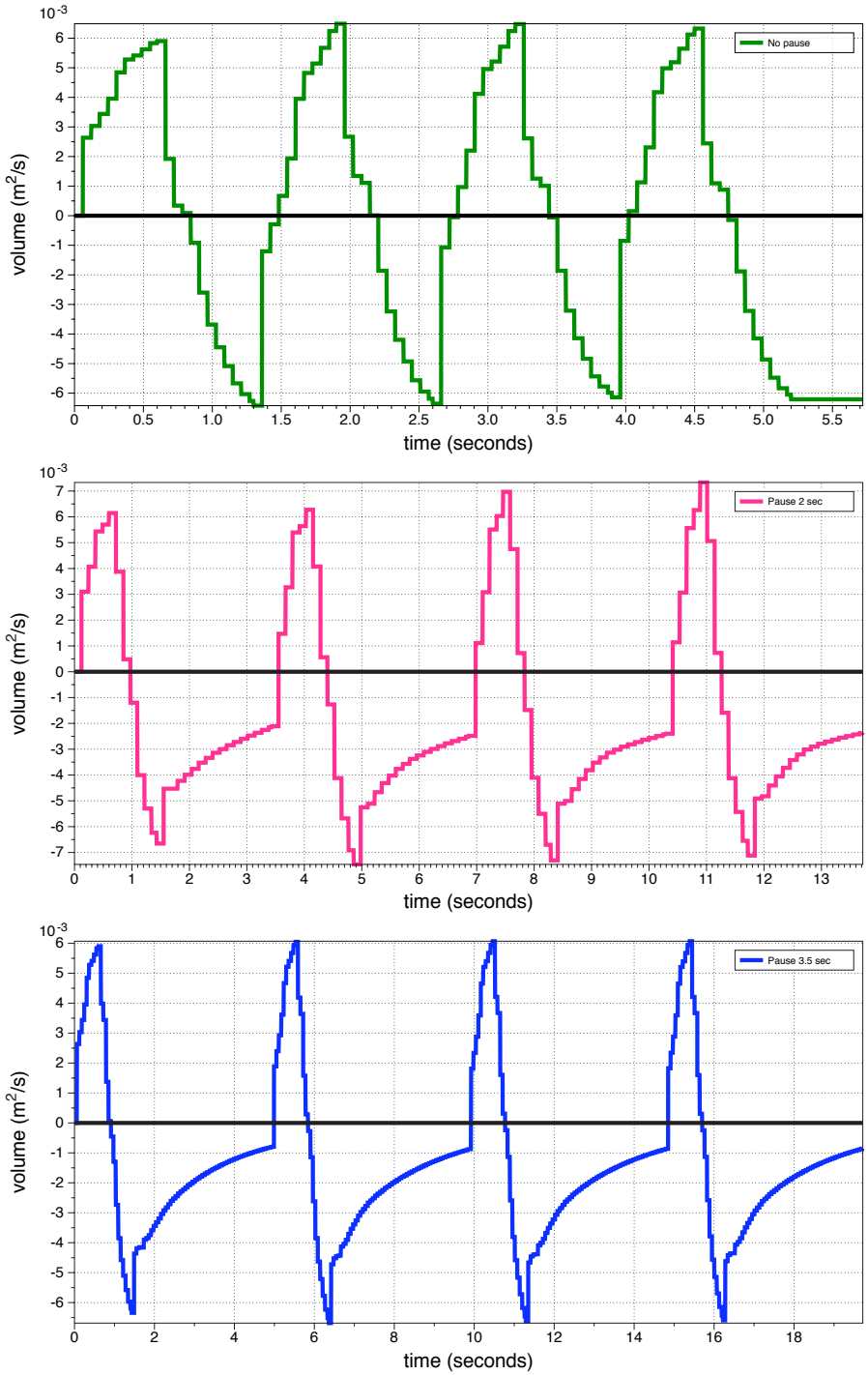

FIGURE 2.15. Volumetric flow rates were compared among simulations of three different porous models. Top: A model with no pauses is shown. Middle: The standard porous model with a pause of 2 seconds between expansion and the following contraction is shown. Bottom: A model with a pause of 3.5 seconds is shown. These plots indicate the normalized horizontal flow from the left of the domain toward the model organism. Positive flow indicates fluid moving toward the structure, while negative flow indicates flow moving away from the structure.

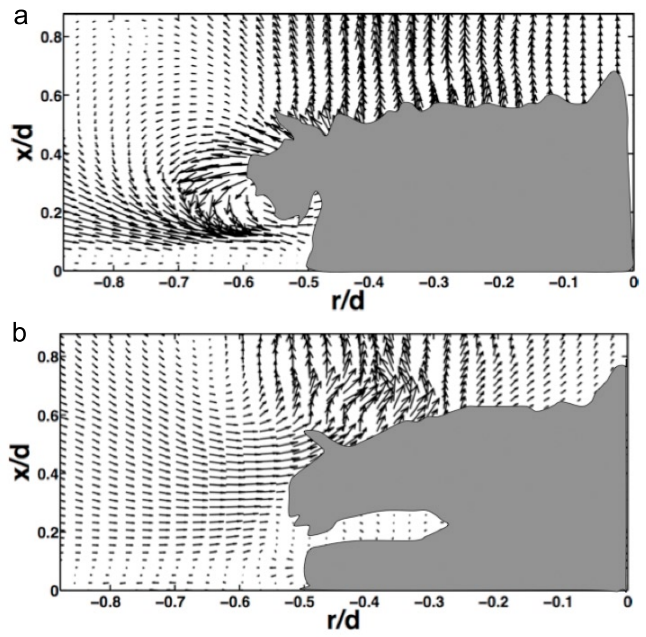

FIGURE 2.16. Phase-locked velocity vector fields of the flow generated by a *C. xamachana* medusa of 6 cm maximum bell diameter using particle image velocimetry. The results shown were obtained by averaging over 10 pulsing cycles, where the positions of the bell and oral arms were identical across all the individual realizations used toward the averaging process. (a) shows the pulsing phase corresponding to full contraction of the bell and (b) shows the phase corresponding to full relaxation of the bell.

CHAPTER 3

A Numerical Study of the Effects of Bell pulsation of the Upside-down Jellyfish *Cassiopea xamachana* on the Currents in Channel Flow

3.1. Introduction

In this section, the jellyfish model developed in the previous chapter was implemented while immersed in a channel flow. Since *C. xamachana* naturally inhabits shallow, low-flow environments it is important to examine the interaction between the pulse of the organism and a low-velocity ambient flow. The goals in this chapter were 1) to continue to investigate whether the addition of a porous secondary structure influences the flow field compared to a more commonly assumed bell-only model; 2) to examine whether relevant ambient flow conditions dominate the effects of the pulsing bell; and 3) examine the effects of pause length on the bulk flow structure. Flow environments in typical *C. xamachana* habitats measured approximately 10 m below the surface of the water have an average maximum velocity on the order of 10 cm/s with lower velocities on the order of 0.1-1 cm/s likely closer to the seafloor [**72, 38, 57, 42, 52, 79**]. Although actual flow experienced by *C. xamachana* is variable in both direction and speed, in this simplified model a constant direction of flow was initially assumed. The constant flows in each simulation were varied from 0.0 to 3.0 cm/s, which was taken as a reasonable approximation of the ambient velocity experienced by the organism. In addition, variable flow simulations were performed with a maximum mid-channel flow velocity of 1.0 cm/s.

3.2. Materials and Methods

3.2.1. Immersed Boundary Method with Channel Flow. A rigid wall on the top and the bottom of the domain was used to simulate the sides of the channel as shown in Figure 3.1. The inflow from the left side to the right side of the domain was simulated using a ramping method described below. The top and bottom of the channel were approximated by target points and boundary points tethered together by stiff springs in

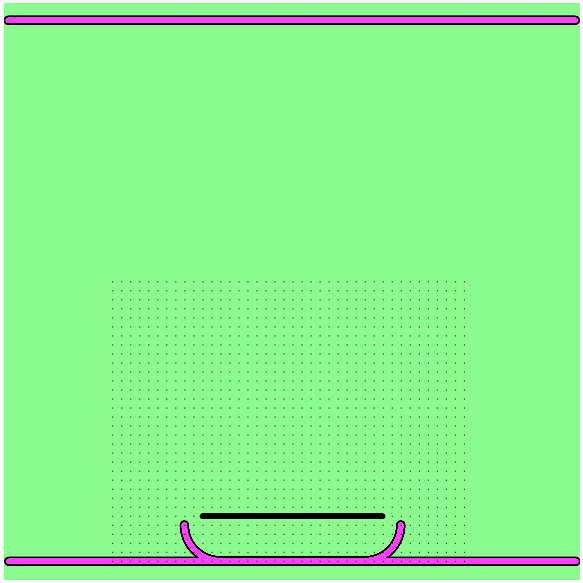

FIGURE 3.1. A cartoon of the channel flow simulation set-up. The top of the fluid domain extends throughout the green area. The channel flow region was between the two horizontal magenta lines. The jellyfish model and porous layer are shown in magenta and black, respectively. The boundaries on the fluid domain were periodic on all sides. Flow was driven from left to right.

the same manner as the box in Chapter 1. The jellyfish model was placed on the bottom wall of the channel (Figure 3.1) and was pulsed using the same linear interpolation described in Chapter 1.The actual fluid domain had periodic boundary conditions along each border. Fluid re-entering the periodic domain from the other side was accounted for by the methods described below. By defining the channel in this way, the fluid equations were solved using Fast-Fourier Transform methods, allowing more rapid computation.

To drive flow in the channel, an external force was applied to the fluid through a term in the Navier Stokes equations, $\mathbf{f}_{ext}$. The force was applied along the height of the channel on a strip 0.33 cm in width and 6.3 cm upstream from the body of the jellyfish. A preferred parabolic profile was defined for flow through the channel. The external force

was determined by

$$\mathbf{f}_{ext} = -k_R \left(\mathbf{u}_t \left(\mathbf{x}, t \right) - \mathbf{u} \left(\mathbf{x}, t \right) \right) \tag{3.1}$$

where $\mathbf{u}_t \left(\mathbf{x}, t \right)$ was the desired flow velocity, $\mathbf{u} \left(\mathbf{x}, t \right)$ was the actual fluid velocity, and k_R was a proportionality constant chosen so that the difference between $\mathbf{u}_t \left(\mathbf{x}, t \right)$ and $\mathbf{u} \left(\mathbf{x}, t \right)$ was less than 0.1%. Equation 1.1 now becomes

$$\rho \left[\frac{\partial \mathbf{u} \left(\mathbf{x}, t \right)}{\partial t} + \mathbf{u} \left(\mathbf{x}, t \right) \cdot \nabla \mathbf{u} \left(\mathbf{x}, t \right) \right] = -\nabla p \left(\mathbf{x}, t \right) + \mu \nabla^2 \mathbf{u} \left(\mathbf{x}, t \right) + \mathbf{f} \left(\mathbf{x}, t \right) + \mathbf{f}_{ext} \tag{3.2}$$

To determine the preferred velocity along the strip, let y_1,y_2 be the y-coordinate of the bottom and of the top of the channel, respectively. Let $U_{max} \left(t \right)$ be the target mid-stream velocity in the x-directon at $y_3 = \frac{y_1 + y_2}{2}$ and time t. The profile along the height of the channel was then determined by

$$u_t \left(x, y, t \right) = \begin{cases} a \left(t \right) \left(y^2 + by + c \right) & \text{inside channel} \\ 0 & \text{outside channel} \end{cases} \tag{3.3}$$

where

$$\begin{aligned} a \left(t \right) &= \frac{U_{max}(t)}{(y_1 - y_3)(y_2 - y_3)} \\ b &= -\left(y_1 + y_2 \right) \\ c &= y_1 y_2 \end{aligned} \tag{3.4}$$

The target velocity in the y-direction was set to zero ($v_t \left(x, y \right) = 0$) along the forced strip region. To avoid shocks and instability from the initialization of channel flow, the mid-channel velocity was linearly ramped from zero to the final desired velocity over 10

seconds. If U_{final} was the final desired mid-channel velocity then at time t during the ramping $U_{max}(t) = \frac{U_{final}}{r}t$. Once the final profile was reached, it was maintained for the remainder of the simulation. As the channel flow exited the periodic domain on the right and re-entered from the left, the forcing strip acted as a virtual "flow straightener" to prevent the periodicity from disrupting the inflow of the channel. This method has been used previously to simulate channel and pipe structures such as arterial walls and the embryonic heart using the IB method [**31, 69**].

3.2.2. Variable flow environments. In addition to the constant velocity flows described above, variable flow environments were examined as well. To vary the flow, instead of increasing the maximum mid-channel velocity in a linear fashion, the mid-channel velocity was determined by changing $a(t)$ in Equation 3.4 so that

$$a(t) = \begin{cases} U_{final}\left(\frac{1+\sin\left(\gamma t - \frac{\pi}{2}\right)}{2}\right) & \text{single direction} \\ \\ U_{final}\left(\sin\left(\gamma t - \frac{\pi}{2}\right)\right) & \text{bi-directional} \end{cases} \tag{3.5}$$

where $\gamma = 2\pi f$ for a given frequency f. In the case of the sinusoidal pulse no ramp was used. Two types of pulse-driven flow were considered. The first type used was single direction flow in which the velocity was allowed to vary from 0 m/s to U_{final} m/s with the fluid traveling from left to right. The second type used was bi-directional flow in which the mid-channel velocity was varied from $-U_{final}$ m/s to U_{final} m/s so that the mid-channel flow direction was sometimes reversed. The frequencies used in both cases were the same.

3.3. Results

The effect of the pulsing kinematics and the presence of porous layer were investigated in channel flow. The parameters used in the simulations were the same as those summarized in Tables 2.1 and 2.2 except that the porosity was set to $\lambda = 0.00000072$. The cases are summarized in Table 3.1.

In this chapter, the flow lines were defined in the same manner and in the same position as in the previous chapter (see Figure 2.4.) The flow rates were displayed for time ranges after the 10 second ramp period. When compared to the sinusoidal cases without a ramp, the values for the variable flow were shifted 10 seconds to the right so that the pulse timings overlap exactly in each case. Examples of the general pattern of flow rates corresponding to each phase of the pulse cycle are given in Figure 3.2. In addition to the HFL on the left (now termed LHFL) a corresponding line on the right termed the RHFL was also defined the same distance from the bell (see Figure 3.3.) The left horizontal flow rate (LHFR) was normalized by dividing by the length of the LHFL while the right horizontal flow rate (RHFR) was normalized by dividing by $-L_r$ where L_r was the length of the RHFL. By normalizing in this manner, positive values always corresponded to flow toward the bell while negative values corresponded to flow away from the bell on either side of the model. In the case of the vertical flow line (VFL), the flow rate was normalized by dividing by the length of the VFL. Positive values corresponded to flow

TABLE 3.1. Values of all parameters in the simulations unless otherwise noted

	Arms No Pause	Arms Pause	No Arms Pause	No Arms No Pause
5 mm/s	16A	1A	12A	2A
1 cm/s	13A	3A	5A	4A
2 cm/s	14A	8A	9A	10A
3 cm/s	11A	15A	7A	6A

away from the bell while negative values corresponded to flow toward the bell. For the HFRs the large increased flow toward the bell corresponded to the beginning of the bell contraction. The decrease of the flow toward the bell occurred during the first pause and the expansion phase. During the second pause (if present), the flow toward the bell slowed and in some cases reversed. During the pauses a gradual increase in flow toward the bell and a plateauing of the flow rate was observed before the next contraction begins. For the VFRs, a similar pattern was observed for flow away from and toward the porous layer.

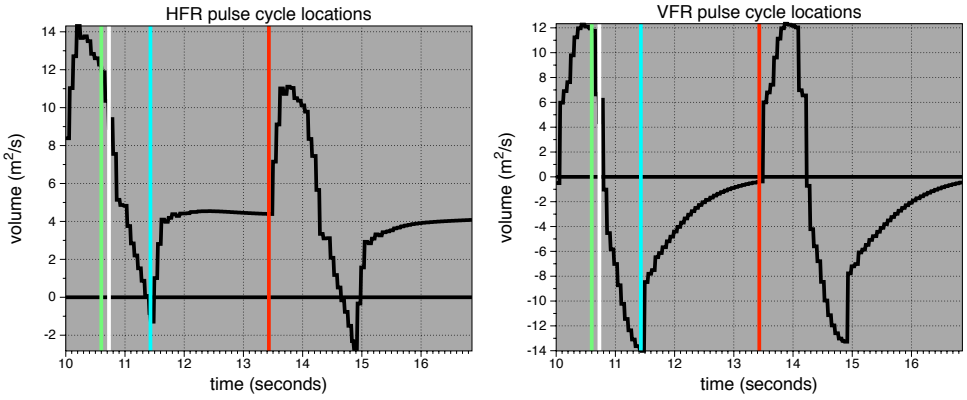

FIGURE 3.2. A diagram of the pattern of the model organism's pulse cycle for the HFR(left) and VFR(right). The cycle starts at the beginning of the domain at 10 seconds. The region between the beginning of the diagram and green line corresponds to the contraction of the model. The region between the green and white lines corresponds to the short pause between contracting and relaxing. The region between the white line and the blue line corresponds to the relaxation of the bell. The region between the blue line and the red line corresponds to the second longer pause at the end of the cycle.

3.3.1. The effect of oral arms. Vorticity plots for cases 1A (porous layer model at 0.5 cm/s) and 12A (bell-only model at 0.5 cm/s) and cases 8A (porous layer model at 2.0 cm/s) and 9A (bell-only model at 2.0 cm/s) are shown in Figures 3.4 and 3.5,

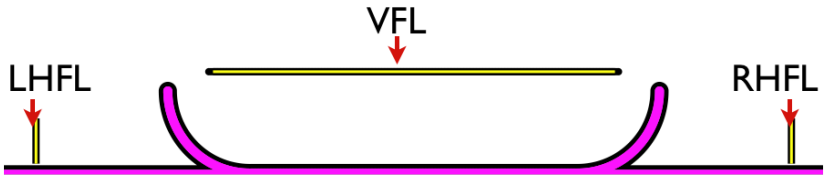

FIGURE 3.3. Positions of the flow lines used to measure the volumetric flow rates around the bell. From left to right the yellow lines are 1) the left horizontal flow line (LHFL) which was 0.4 L to the left of the outside of the bell; 2) the vertical flow line (VFL) which was drawn on top of the porous layer of the left model; 3) the right horizontal flow line (RHFL) which was 0.4 L to the right of the outside of the bell.

respectively, as representative of the various flow profiles. Flow in the channel for each case was from left to right. For all simulations the initial vortex forming at the tip of the bell was slightly larger on the downstream (right) side of the bell. In the porous layer model the vortices were trapped and directed along the top of the layer. In the bell-only model the vortices generated on the right side were quickly advected away from the bell. On the upstream (left) side of the bell, the vortices directed the flow upward and away from the arm region.

Figure 3.6 shows the LHFR for cases with pauses (Cases 2A, 10A, 14A and 16A) at flow speeds of 0.5 cm/s and 2.0 cm/s. Notice the increase in the peak values and the total LHFR as the maximum mid-channel velocity increased for each case. The VFR for the same cases is shown in Figure 3.7. There was little change in the exchange across the oral arm region in the cases with oral arms and slightly more variation in the amount of flow toward the bell and the amount of backflow away from the bell in the cases without arms. In the latter cases, as the velocity increased the flow toward the bell increased during the contraction and relaxations while the amount of backflow decreased with increasing velocity. The HFR on the right of the bell is shown in Figure

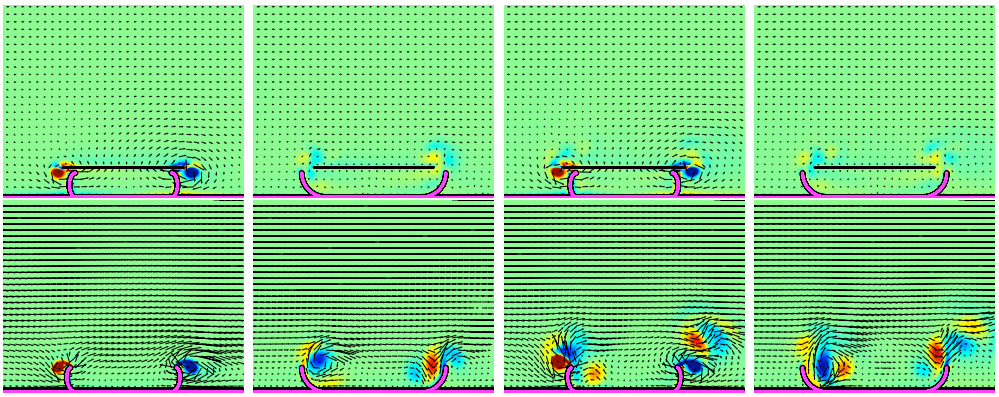

FIGURE 3.4. Vorticity plots at 0.5 cm/s with pauses from numerical simulations with overlain velocity vector fields. Warm colors show regions of positive vorticity while cool colors are areas of negative vorticity. Top, left to right: vorticity plots for the porous model at the first contraction, the first full cycle, the fourth contraction, and the fourth full cycle. Bottom, left to right: Vorticity plots for the armless model at the corresponding stages of pulsing.

3.8. The cases with arms (Cases 1A and 8A shown) converged quickly to a similar flow pattern. In the cases without arms (Cases 2A and 10A shown.) the flow toward the bell during contraction increased and the backflow during the pauses continued to decrease with increasing channel velocity. From the vorticity plots in Figures 3.4 and 3.5 the flow

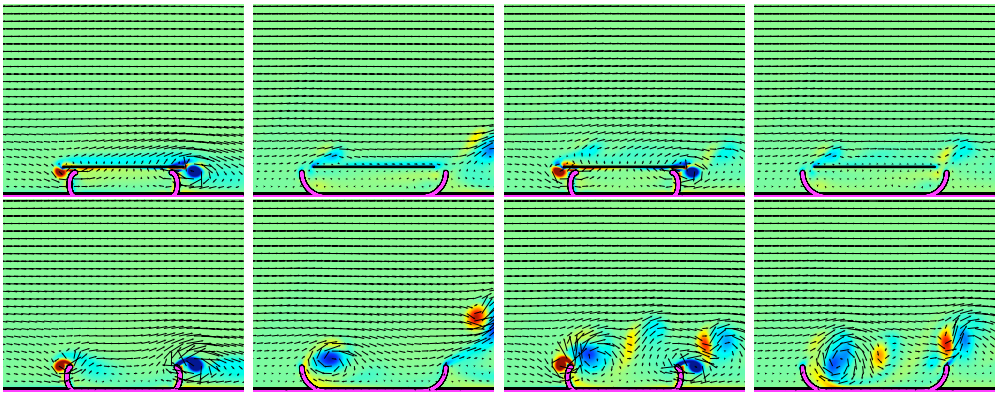

FIGURE 3.5. Vorticity plots at 2.0 cm/s with pauses from numerical simulations with overlain velocity vector fields. Warm colors show regions of positive vorticity while cool colors are areas of negative vorticity. Top, left to right: vorticity plots for the porous model at the first contraction, the first full cycle, the fourth contraction, and the fourth full cycle. Bottom, left to right: Vorticity plots for the armless model at the corresponding stages of pulsing.

in the porous layer model trapped within the vortex attached to the layer and directed across it. In the bell-only model, the vortices were advected away from the structure, driving the flow in different directions. The particles advected to the right side of the bell and those located in the sheltered region downstream of the bell would be less likely to be advected toward the bell for sampling. On the left of the bell, the HFR for the porous layer models and the bell-only models each converged to a similar pattern. There was little qualitative difference in the flow rates in each of the cases in low flow conditions. The velocity of the fluid being driven across the region was lower in the porous case versus the bell-only case based on the vector field plots in Figures 3.4 - 3.10.

3.3.2. The effect of pauses. Vorticity plots for cases 2A (no arms and no pauses) and 16A (arms and no pauses) at 0.5 cm/s and cases 10A (no arms and no pauses) and 14A (arms and no pauses) at 2.0 cm/s are shown in Figures 3.9 and 3.10. Flow in the channel for each case was from left to right. For 0.5 cm/s background flow without arms, the vortices are advected toward the center of the bell and upwards on the downstream end. For the same case with the porous layer, the vortices move across the oral arms and are not transported away from the organism as quickly. For 2.0 cm/s background flow without arms, starting and stopping vortices are quickly advected downstream. The addition of the oral arms slows the downstream transport of the vortices, allowing longer sampling times.

The RHFR and VFR for the cases with no pauses at each flow speed (Cases 9, 12, 14, and 16) are given in Figures 3.11,and 3.12, respectively. In the bell-only cases (Cases 2A and 10A) the RHFR in Figure 3.11 changes dramatically in both magnitude and pattern as channel speed increased. The magnitude of the exchange across the oral

arm region given by the VFR in Figure 3.12 was larger in the case of the bell-only model. The exchange pattern remained the same across channel flows for both the porous model case and the bell-ony case.

The flow on the right (Figure 3.11) in the case of both the porous layer and bell-only simulations shows flow rates for both the porous models and the bell-only models increasing as the mid-channel velocity increased. The pattern of the pulse was similar between the 0.5 cm/s case and the 2.0 cm/s case in the porous layer models. The pattern in the bell-only cases changes considerably as the mid-channel velocity increased from 0.5 cm/s to 2.0 cm/s. The vorticity plots (Figures 3.9 and 3.10) showed the vortices formed at the tip of the bell on the right side were advected strongly upward outside of the the porous layer region before being transported away from the bell by the channel flow. This trend increased as the mid-channel velocity increased. In the case of the porous layer models, the vortices were trapped in the oral arm region by the porous layer for a period of time before being advected away.

Examining the left flows in Figures 3.9 and 3.10 the vortices persisted in the region of the porous layer in the bell-only case. The vortices drove the fluid approaching from the left upward away from the oral arm region, decreasing the amount of flow from the substrate that actually reached the presumed exchange region. In the case of the porous models, the vortices were again trapped around the edge of the bell and drove the fluid toward and across the oral arm region. The VFRs shown in Figure 11 showed the exchange across the porous layer was similar in pattern and magnitude in both the porous layer model and the bell-only model.

3.3.3. The effect of variable flow. A frequency of $f = 3/t_{tot}$ (~ 0.22 Hz), where t_{tot} was the total time of the simulations, was chosen for the sinusoidal pulsing simulations. This was within the range of observed frequencies for some low velocity flows in *Cassiopea* habitats (~ 0.05 to 0.3 Hz) [**34, 45**].The LHFR and RHFR for the pulsed cases with a maximum mid-channel velocity of 1.0 cm/s are given in Figures 3.13 and 3.14, respectively. There are four pulses with the same cycle timing as the other simulations with pauses and constant flow although the pattern was less clear in these figures. The VFR for the pulsed cases is given in Figure 3.15. The HFRs in Figures 3.13 and 3.14 showed a very irregular pattern, while the VFRs in Figure 3.15 showed a regular exchange rate pattern similar to those seen in the constant channel flow cases. Vorticity plots for bi-directional flow for porous layer models and bell-only models are shown in Figure 3.19. The vortices were directed toward the porous layer while in the bell-only model the vortices were advected back and forth above the bell. In the bell-only model, the vortices were also advected upward and away from the bell as they move back and forth. In the porous layer model, the vortices linger longer in the oral arm region.

The flow rates in the variable mid-channel velocity cases deviated noticeably from the flow rates in the constant mid-channel case with the same maximum channel velocity of 1.0 cm/s as seen in Figures 3.16, 3.17, and 3.18. The pattern of the horizontal flow rates for the variable flows was very similar in porous layer and bell-only models, although the flow toward the bell was greater in the case without arms. The vorticity plots in Figure 3.19 showed the porous layer serves to trap vortices which directed flow across the porous layer. Without the porous layer the vortices circulated around the inside of the bell, upwards away from the bell, and back and forth on the inside of the bell. As in

the constant flow cases the oral arm structure did not enhance transport in the porous layer region as seen in Figure 3.18, but the porous layer did serve to trap the vortices so that the flow was directed more smoothly across the porous layer with less recirculation of the same fluid.

3.4. Discussion

The results presented in this chapter indicate 1) the porous structure alters the flow around the bell compared with bell-only models in such a way that fluid was continually driven across and through the porous layer for sampling; 2) the porous structure traps the vortices as they form on either side of the bell tips and directed the flow more gently across and through the porous layer compared to bell-only models which showed large swirling vortices which were more quickly advected away as the flow speeds in the channel increase; and 3) in variable flow the porous layer again traps the forming vortices so that fluid is directed toward the arm region instead of being advected upward as in seen in the bell-only model. The addition of the porous structure to the bell-only jellyfish model thus dramatically changes the character of the flow patterns in most cases.

The key feature observed in each of these cases was that the vortex formation and shedding was highly variable in the bell-only models, while the pattern of flow across and through the porous layer was more similar across a range of simulations. Assuming that the organism requires some time for particle transfer and sampling for food to be effective, the lower vorticity and more diffuse spreading of the vortices across the oral arm region would be advantegeous for feeding. Although there may be some cases in which a morphology corresponding to the bell-only model (*i.e.* a large prominent bell with relatively negligible tentacles or oral arms) may promote more efficient flow patterns for

feeding, morphologies simulated by the porous layer model (in which the oral arms were a prominent feature of the organism) appear to offer a similar pattern for feeding across a wider range of flow profiles which may be advantageous for sampling in a variable flow environment.

As seen in Figure 3.7 the VFRs were greater in the bell-only simulation in the region where the oral arms would be present. Examining the vorticity plots in Figures 3.4 and 3.5, the VFR was largely accounted for by the noticeable vorticity on the left side of the bell. This suggests that the exchange was occurring on one side of the bell resulting in sampling only from the upstream area of the bell. This suggests the presence of the porous structure was important not only in directing flow toward the bell in low flow conditions but also in directing it across the porous layer for sampling. This type of flow trapping may increase the amount of time the organism would have to sample for particles before being removed from the reach of the organism. Since particle capture is not an instantaneous process, the lower flow rates in the arm area may allow more efficient sampling of fluid.

The HFR on the right of the bell shown in Figure 3.8 exhibits a similar pattern, with the porous layer case exhibiting a lower flow rate than the bell-only model. Examining the vorticity plots in Figures 3.4 and 3.5 again, it was seen in the bell-only case that as the channel speed increases more of the fluid is advected away from the bell as soon as it leaves the region sheltered by the structure. Fluid advected away in the porous layer model, but the trapped vortex along the tip of the porous layer drives some of the fluid across the oral arm region. As flow speed increases, the presence of a prominent structure helps to trap some fluid around the oral arms for sampling. This suggests that

the presence of the porous layer tends to keep the flow adjacent to the bell in about the same range compared to the bell-only model as the channel flow increases.

The porous layer does not affect the horizontal flow rate on the left of the bell substantially in channel flow both with and without pauses as seen in Figures **??** and 3.6. In the absence of pauses there was more fluid driven toward the bell overall in the bell-only model. The porous layer traps the vortices in a pattern that directs a more gentle flow toward the feeding region in a way that could promote better sampling. Combining this with the observations that more flow from the substrate was directed toward the arm region suggests that particle sampling was more effective in the porous layer model.

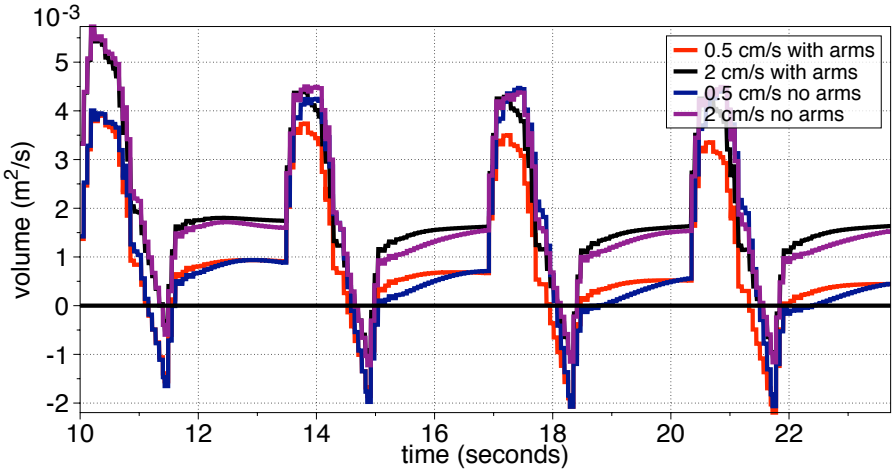

FIGURE 3.6. Volumetric flow rates along the LHFL describing horizontal flow moving towards the bell from the left were compared among simulations of four different models with 2.0s pauses between pulse cycles. The porous model with a mid-channel velocity of 0.5 cm/s is shown in red while the porous model with a mid-channel velocity of 2.0cm/s are shown in black. Models without porous layers at 0.5 cm/s and 2.0cm/s are shown in blue and purple, respectively. These plots indicate the normalized horizontal flow from the left of the domain toward the model organism. Positive flow indicates fluid moving toward the structure, while negative flow indicates flow moving away from the structure.

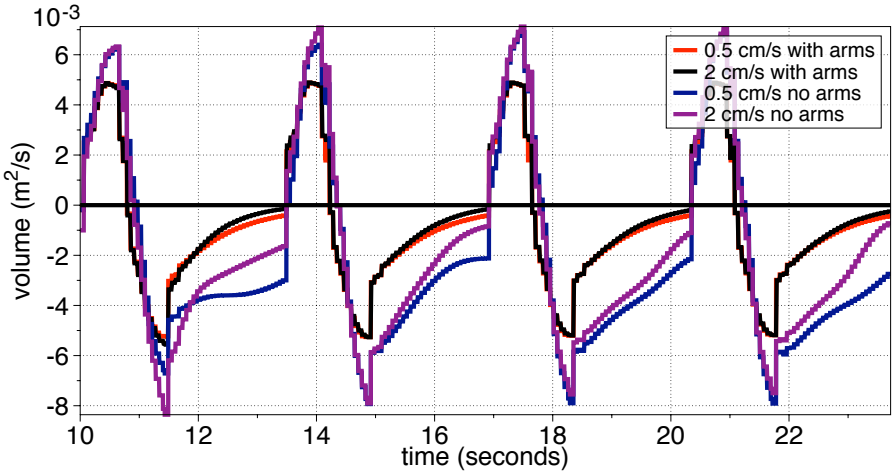

FIGURE 3.7. VFR across oral arms Volumetric flow rates along the VFL describing vertical flow moving across the region of the porous layer location were compared among simulations of four different models with 2.0s pauses between pulse cycles. The porous model with a mid-channel velocity of 0.5 cm/s is shown in red while the porous model with a mid-channel velocity of 2.0cm/s are shown in black. Models without porous layers at 0.5 cm/s and 2.0cm/s are shown in blue and purple, respectively. These plots indicate the normalized vertical flow across the porous layer region toward the model organism. The flows have been normalized in such a way so that positive flow indicates fluid moving away from the structure, while negative flow indicates flow moving toward the structure.

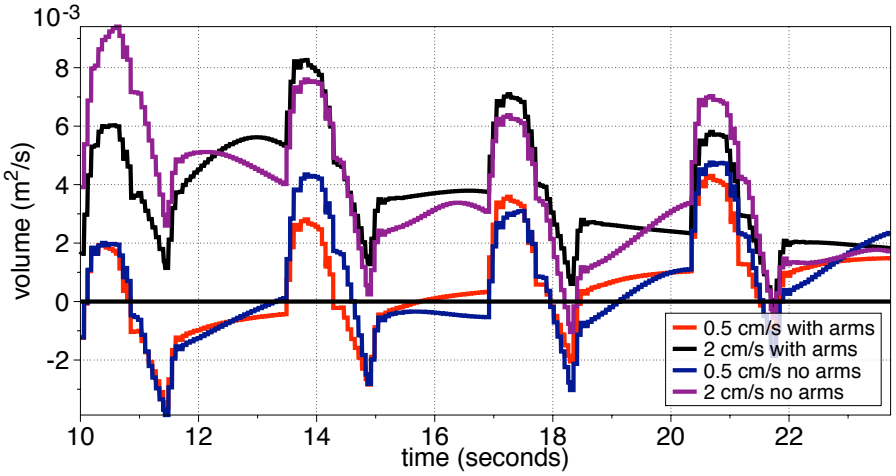

FIGURE 3.8. Volumetric flow rates along the RHFL describing horizontal flow moving towards the bell from the right were compared among simulations of four different models with 2.0 pauses between pulse cycles. The porous model with a mid-channel velocity of 0.5 cm/s is shown in red while the porous model with a mid-channel velocity of 2.0cm/s are shown in black. Models without porous layers at 0.5 cm/s and 2.0cm/s are shown in blue and purple, respectively. These plots indicate the normalized horizontal flow from the right of the domain toward the model organism. The flows have been normalized in such a way so that positive flow indicates fluid moving toward the structure, while negative flow indicates flow moving away from the structure.

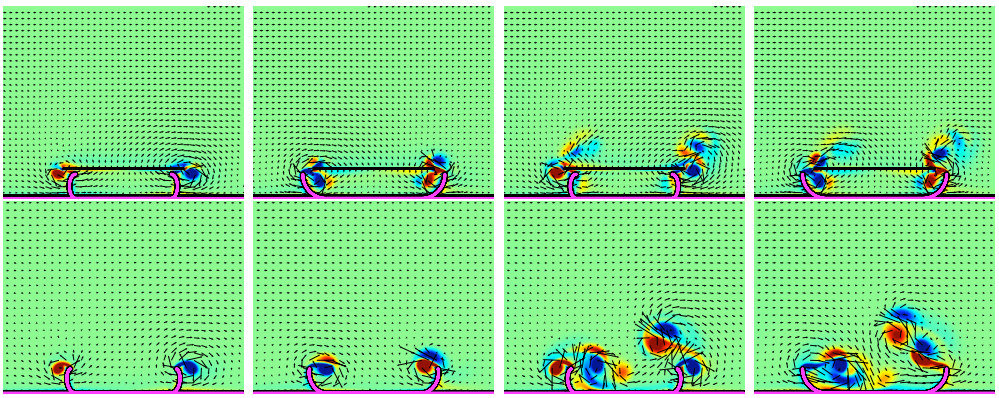

FIGURE 3.9. Vorticity plots at 0.5 cm/s with no pauses from numerical simulations with overlain velocity vector fields. Warm colors show regions of positive vorticity while cool colors were areas of negative vorticity. Top, left to right: vorticity plots for the porous model at the first contraction, the first full cycle, the fourth contraction, and the fourth full cycle. Bottom, left to right: Vorticity plots for the armless model at the corresponding stages of pulsing.

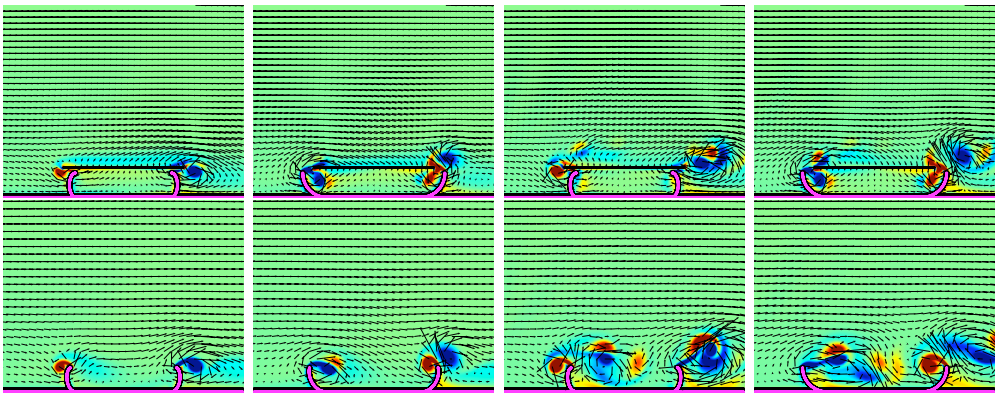

FIGURE 3.10. Vorticity plots at 2.0 cm/s with no pauses from numerical simulations with overlain velocity vector fields. Warm colors show regions of positive vorticity while cool colors were areas of negative vorticity. Top, left to right: vorticity plots for the porous model at the first contraction, the first full cycle, the fourth contraction, and the fourth full cycle. Bottom, left to right: Vorticity plots for the armless model at the corresponding stages of pulsing.

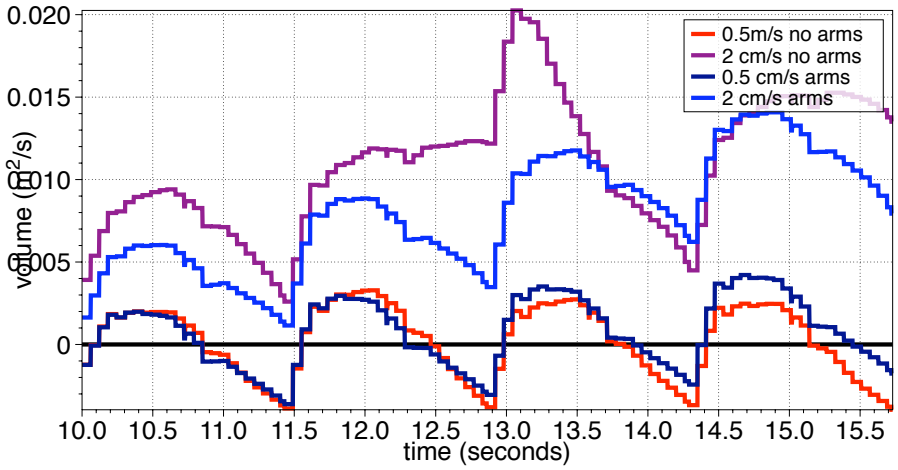

FIGURE 3.11. Volumetric flow rates along the RHFL describing horizontal flow moving towards the bell from the right were compared among simulations of four different models with no pauses between pulse cycles. The porous model with a mid-channel velocity of 0.5 cm/s is shown in red while the porous model with a mid-channel velocity of 2.0cm/s are shown in black. Models without porous layers at 0.5 cm/s and 2.0cm/s are shown in blue and purple, respectively. These plots indicate the normalized horizontal flow from the right of the domain toward the model organism. The flows have been normalized in such a way so that positive flow indicates fluid moving toward the structure, while negative flow indicates flow moving away from the structure.

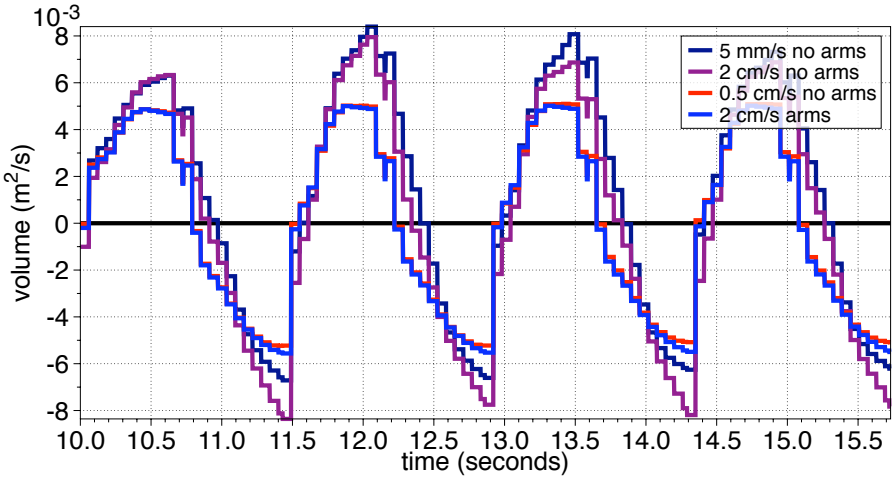

FIGURE 3.12. VFR across porous layer Volumetric flow rates along the VFL describing vertical flow moving across the region of the porous layer location were compared among simulations of four different models with no pauses between pulse cycles. The porous model with a mid-channel velocity of 0.5 cm/s is shown in red while the porous model with a mid-channel velocity of 2.0cm/s are shown in black. Models without porous layers at 0.5 cm/s and 2.0cm/s are shown in blue and purple, respectively. These plots indicate the normalized vertical flow across the porous layer region toward the model organism. The flows have been normalized in such a way so that positive flow indicates fluid moving away from the structure, while negative flow indicates flow moving toward the structure.

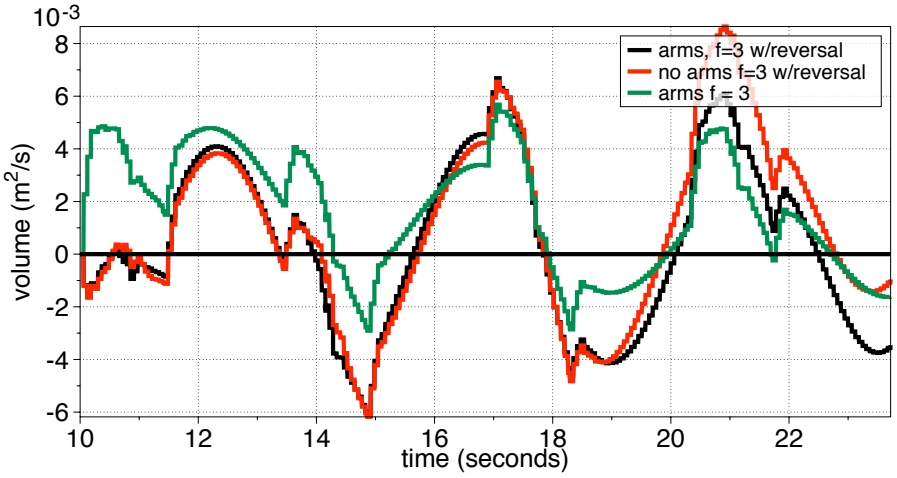

FIGURE 3.13. Volumetric flow rates along the LHFL describing horizontal flow moving towards the bell from the left were compared among simulations of three different models at a maximum mid-channel velocity of 1.0 cm/s with a sinusoidal pulse frequency of f=3.0/(total time of simulation). The porous model with bi-directional flow is shown in black while the porous model with a one-directional flow is shown in green. The bell-only model in a bi-directional flow is shown in red. These plots indicate the normalized horizontal flow from the left of the domain toward the model organism. The flows have been normalized in such a way so that positive flow indicates fluid moving toward the structure, while negative flow indicates flow moving away from the structure.

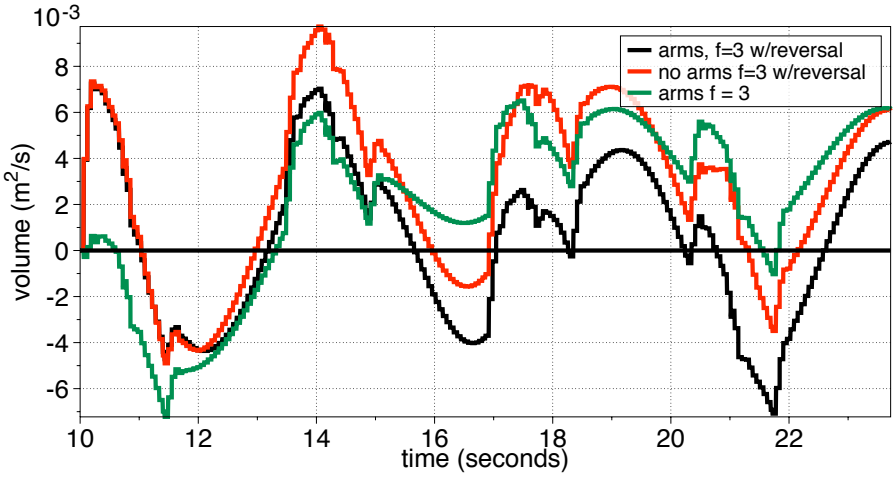

FIGURE 3.14. Volumetric flow rates along the RHFL describing horizontal flow moving towards the bell from the right were compared among simulations of three different models at a maximum mid-channel velocity of 1.0 cm/s with a sinusoidal pulse frequency of f=3.0/(total time of simulation). The porous model with bi-directional flow is shown in black while the porous model with a one-directional flow is shown in green. The bell-only model in a bi-directional flow is shown in red. These plots indicate the normalized horizontal flow from the right of the domain toward the model organism. The flows have been normalized in such a way so that positive flow indicates fluid moving toward the structure, while negative flow indicates flow moving away from the structure.

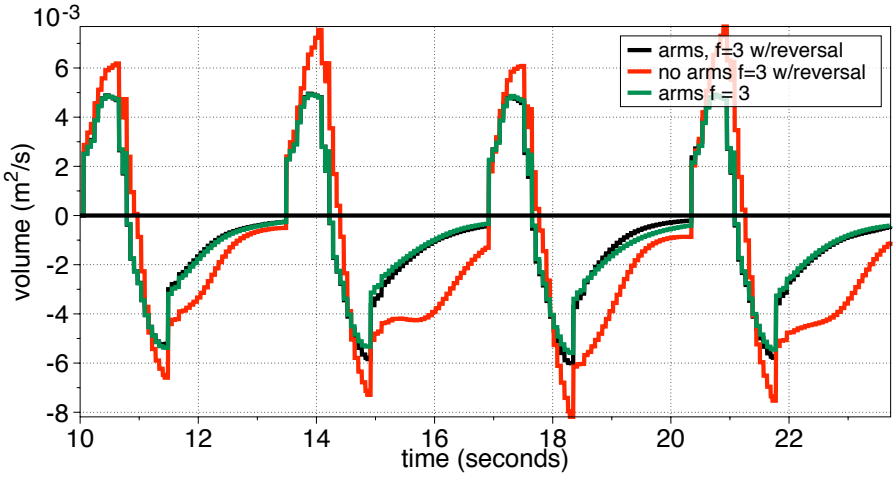

FIGURE 3.15. Volumetric flow rates along the VFL describing vertical flow moving across the porous layer region were compared among simulations of three different models at a maximum mid-channel velocity of 1.0 cm/s with a sinusoidal pulse frequency of f=3.0/(total time of simulation). The porous model with bi-directional flow is shown in black while the porous model with a one-directional flow is shown in green. The bell-only model in a bi-directional flow is shown in red. These plots indicate the normalized vertical flow across the porous layer region toward the model organism. The flows have been normalized in such a way so that positive flow indicates fluid moving away from the structure, while negative flow indicates flow moving toward the structure.

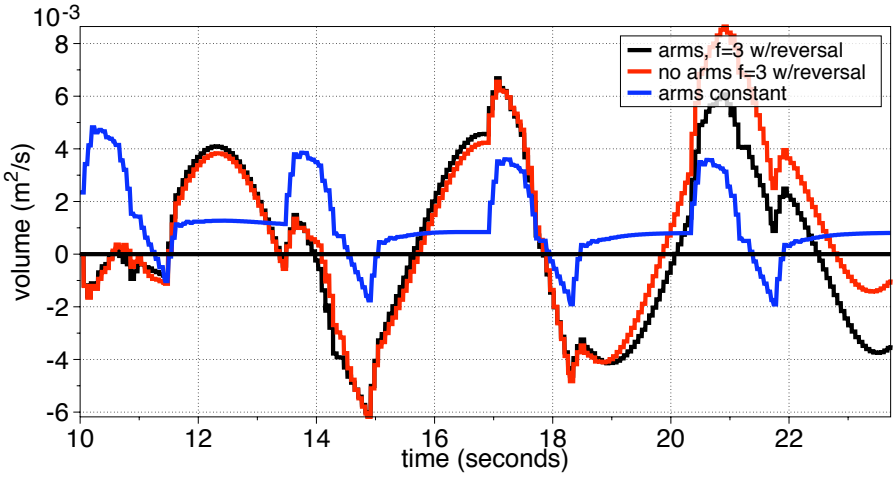

FIGURE 3.16. Volumetric flow rates along the LHFL describing horizontal flow moving towards the bell from the left were compared among simulations of three different models at a maximum mid-channel velocity of 1.0 cm/s with a sinusoidal pulse frequency of f=3.0/(total time of simulation). The porous model with bi-directional flow is shown in black while the porous model with a constant flow is shown in blue. The bell-only model in a bi-directional flow is shown in red. These plots indicate the normalized horizontal flow from the left of the domain toward the model organism. The flows have been normalized in such a way so that positive flow indicates fluid moving toward the structure, while negative flow indicates flow moving away from the structure.

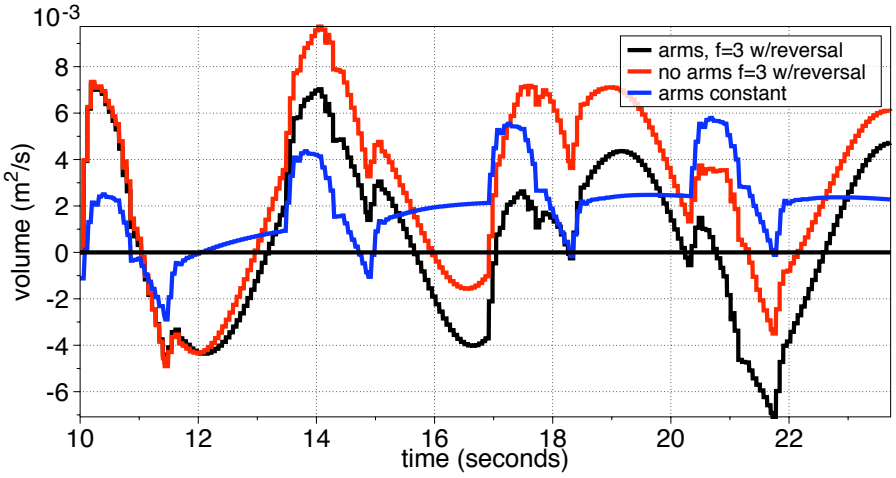

FIGURE 3.17. Volumetric flow rates along the RHFL describing horizontal flow moving towards the bell from the right were compared among simulations of three different models at a maximum mid-channel velocity of 1.0 cm/s with a sinusoidal pulse frequency of f=3.0/(total time of simulation). The porous model with bi-directional flow is shown in black while the porous model with a constant flow is shown in blue. The bell-only model in a bi-directional flow is shown in red. These plots indicate the normalized horizontal flow from the right of the domain toward the model organism. The flows have been normalized in such a way so that positive flow indicates fluid moving toward the structure, while negative flow indicates flow moving away from the structure.

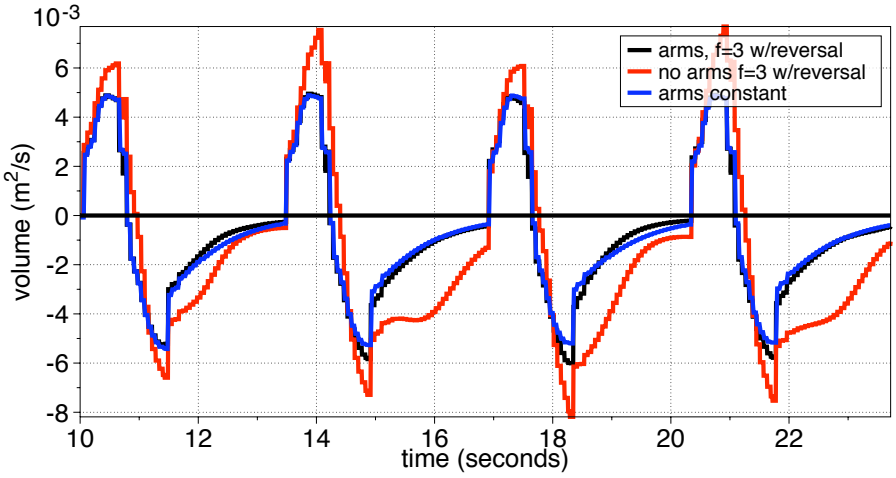

FIGURE 3.18. Volumetric flow rates along the VFL describing vertical flow moving across the porous layer region were compared among simulations of three different models at a maximum mid-channel velocity of 1.0 cm/s with a sinusoidal pulse frequency of f=3.0/(total time of simulation). The porous model with bi-directional flow is shown in black while the porous model with a constant flow is shown in blue. The bell-only model in a bi-directional flow is shown in red. These plots indicate the normalized vertical flow across the porous layer region toward the model organism. The flows have been normalized in such a way so that positive flow indicates fluid moving away from the structure, while negative flow indicates flow moving toward the structure.

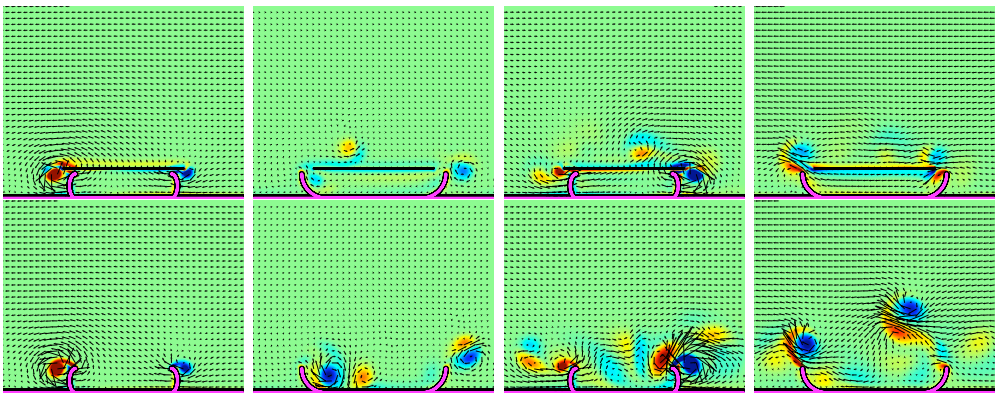

FIGURE 3.19. Vorticity plots at 1.0 cm/s with a sinusoidal pulse frequency of f=3.0/(total time of simulation) from numerical simulations with overlain velocity vector fields. Warm colors show regions of positive vorticity while cool colors are areas of negative vorticity. Top, left to right: vorticity plots for the porous model at the first contraction, the first full cycle, the fourth contraction, and the fourth full cycle. Bottom, left to right: Vorticity plots for the armless model at the corresponding stages of pulsing.

CHAPTER 4

A Study of the Effects of Random Pulses and Multiple Jellyfish Models on Flow around and through the Porous Structures

4.1. Introduction

In the previous chapters models of individual jellyfish with constant cycle periods were examined. In this chapter the effects of variable cycle periods and neighboring individuals on the flow of fluid around the bell are examined. This work was motivated by field and laboratory observations of grouping behavior. While some prefer to remain solitary, some individuals in laboratory aquaria were often observed to reposition themselves into groups, particularly those individuals that appeared weakened or unhealthy. In the field, such as in Grassy Key, Florida, *Cassiopea* have been observed in both solitary and grouped configurations (personal observations, also [**75, 57, 83**]). In order to examine the effect of neighboring individuals, it was necessary to consider the timing of the pulses and to construct more realistic models of organisms in close proximity.

The contraction and expansion times are regulated by muscle mechanics and material properties of the bell which are relatively invariant, but the length of time between the end of expansion and the beginning of the next contraction can vary dramatically. As a result, the laboratory specimens in close proximity to one another were observed to pulse in synchronous, asynchronous, and antisynchronous patterns at various times. To understand the effect of pulse timing for multiple organisms, models of randomly pulsed jellyfish were simulated using the IB method.

The types of pauses between relaxation and subsequent contraction were loosely categorized as "long" pauses and "short" pauses. Analysis of video recordings suggested that short term transitions between the two types of pauses was dependent primarily on the current state. Making the assumption that the length of the next pause is entirely dependent on the length of the current pause allowed the second pause to be modeled

as a discrete time Markov (DTM) process, that is as a chain of random processes which follow the Markov property. Developed in 1907 by A. A. Markov, Markov processes are stochastic processes in which the outcome probability is determined only by the current state of the system and is independent of past states [**32**].

Using the probabilities based on experimental data, a series of pulses were generated using a Markov matrix. These pulse times can be used to simulate the stochastic behavior observed in natural jellyfish. This type of Markov modeling allowed the study of the effect of variable pulses on the flow field around the jellyfish using a pulse pattern that approximated live jellyfish without enforcing a regular pattern over a long period of time. This was a simplifying assumption in that the lengths of the pauses were likely to be affected by environmental factors such as light, nutrients, and temperature. This was a reasonable first approximation to capture the general effects of variable pauses on flow fields around the bell.

4.2. Materials and Methods

4.2.1. Measurements. Five (5) individuals were filmed for a combined total of 1080 cycles that were used to determine the length of each phase of the jellyfish pulse. During the observations, individuals arranged themselves in different grouping patterns. Lab specimens were observed in a range from isolated($>$ 20 cm away from other individuals) to adjacent with parts of their oral arms or bells overlapping. While grouped closely together ($< 5cm$), the individuals were sometimes observed to pulse in unison. The means and standard deviations of the contraction, first pause, and expansion times were $0.62 \pm 0.052s$, $0.13 \pm 0.04s$, and $0.69 \pm 0.12s$, respectively. A single individual was used to generate the Markov matrices used here. The pause between the end of perceivable

motion after relaxation and the next bell contraction varied considerably. The pauses were distributed in a bimodal distribution pattern as seen in Figure 4.1. A threshold

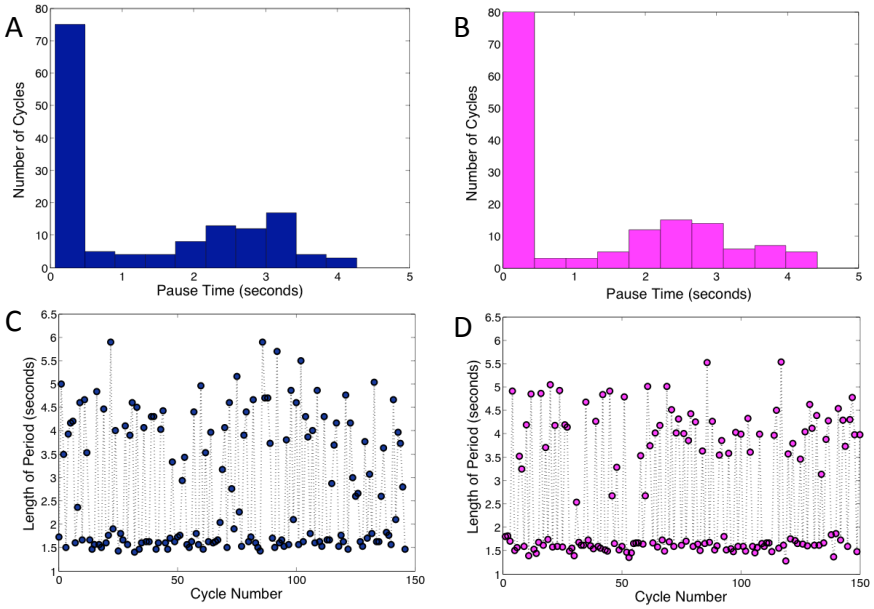

FIGURE 4.1. Experimentally observed and simulated times for the lengths of the pauses between bell expansion and the subsequent bell contraction. The experimental data is shown in A) and C) while simulated data is displayed in B) and D). A histogram showing the frequency of the total cycle lengths A) recorded over 150 cycles for a single medusa and B) simulated using the Markov model. Sequences of pause times C) observed from the same specimen and D) simulated over the course of 150 pulse cycles

was chosen by identifying the pause time between the two largest peaks with the lowest frequency was used to partition the data into short and long pause times.

TABLE 4.1. Pause times for recordings of jellyfish. Note that Individuals 2,3, and 4 were filmed as a group.

Individual	# of cycles	Long Pause (s)	Short Pause (s)	P_{sl}	P_{ls}
1	146	2.59 ± 0.79	0.20 ± 0.11	0.55	0.62
2	247	1.56 ± 0.88	0.20 ± 0.17	0.17	0.82
3	240	2.17 ± 1.12	0.16 ± 0.16	0.20	0.90
4	359	2.17 ± 1.29	0.15 ± 0.13	0.13	0.60
5	88	2.59 ± 0.62	0.46 ± 0.14	0.35	0.70

4.3. Construction of the model

4.3.1. Markov model. The cycle lengths and pause times for an example of pulse cycles generated via a discrete time Markov process are shown in Figure 4.1 with the corresponding data taken from actual medusae. Basing the probabilities on video recordings taken concurrently over a short time minimized the effect in environmental conditions.

The distribution of pause times in each partition was approximated as Gaussian and the means and standard deviations were then calculated. The probability of transitioning from one state to another was determined by summing the number of pairwise transitions observed and dividing by the total number of cases. The probabilities for five individuals are given in Table 4.1. The four transition probabilities were termed P_{ss} (short to short), P_{sl} (short to long) , P_{ls} (long to short), and P_{ll} (long to long). The means, standard deviations and transition probabilities for each partition for five (5) individuals are summarized in Table 4.1. Each simulation began with the jellyfish in the relaxed state. A random starting pulse state was chosen for the first cycle with a randomly chosen time from the range in the current pause state. The Markov matrix was used to determine if a long or short pause occurs in the next cycle. Pulsing dynamics of subsequent cycles were simulated by iteratively applying the Markov matrix to determine the state and randomly selecting a pause time from the appropriate distribution assuming a Gaussian distribution across the range of the partition, forming a chain of pause times.

4.3.2. Multiple jellyfish model. To examine the effect of neighboring organisms, two jellyfish models were placed side by side in the fluid domain. The size of the domain was increased to eight (8) times the length L of the jellyfish bottom. In the first set of simulations two jellyfish models were each placed symmetrically spaced $L/8$ from the

center of the box floor ($L/4$ apart, see Figure 4.5). Simulations were performed to test the effect of pause times, pause synchronization, model organism spacing and model organism size on the flow rates and structures around each bell. To test spacing effects, the pair of jellyfish models were also placed $L/8$ apart and $L/2$ apart. To test the effect of pulse timing a combination of constant and random pauses was used. Finally to test the effect of relative size a smaller jellyfish was placed next to a standard sized one.

4.4. Results

The parameters for these simulations are given in Tables 4.2 and 4.3. The most notable difference from the simulations discussed previously was the increase in the domain size for the multiple jellyfish. The size of the fluid domain was increased from $4L$ to $8L$ in order to minimize wall effects in the simulations while the number of grid points was kept at 512x512.

TABLE 4.2. Values of all parameters in the simulations for the individual Markov simulations and the multiple jellyfish simulations unless otherwise noted.

Parameter	Value
Density $[\rho]$ (kg/m3)	998
Body Length $[L]$ (m)	0.0508
Porosity coefficient $[\lambda]$	0.00000072
Cycle period $[t_1 + t_3 - t_2]$ (s)	1.3
Duty cycle $[t_1/t_4]$	0.4615
1st pause $[t_2 - t_1]$ (s)	0.13
2nd pause* $[t_4 - t_3]$ (s)	2.0
Total period $[t_4]$	3.43

4.4.1. Individual Markov process model. Pause times for the second pause for three different jellyfish simulations were generated using the probabilities from Individual 1 given in Table 4.1. The pause times for each simulation are given in Table 4.4. Passive

TABLE 4.3. Default values of all parameters in the simulations unless otherwise noted. Most notably the 2nd pause varies according to times in Table 4.4, Case 3, in the cases where random pauses were used.

Numerical Parameter	Value
timestep $[dt]$ (s)	0.00006096
Cartesian grid spatial step $[h]$ (m)	0.00079375
Lagrangian spatial step $[ds]$	0.000396876
Domain size (m)	0.4064
Stiffness coefficient, bell and box $[k]$ (N/m)	13987028
Stiffness coefficient, porous layer $[k_p]$ (N/m)	139870.28
Fluid grid size	512 x 512

tracers allowed to move at the local fluid velocity were added as vertical lines of points at the beginning of the simulation.

Each simulation was allowed to run for a total of 12 pulse cycles. The flow rates for the simulations are given in Figures 4.2 and 4.3. A representative vorticity plot of the

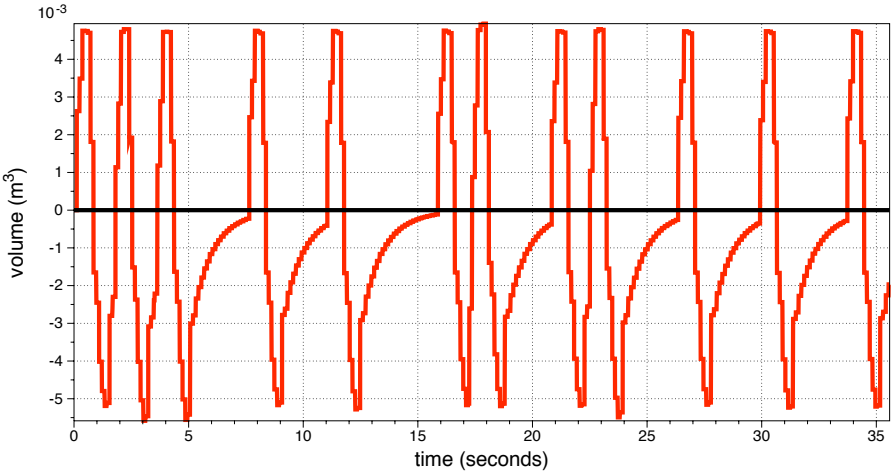

FIGURE 4.2. VFR across oral arms Volumetric flow rates along the VFL describing vertical flow moving across the region of the porous layer location were compared among simulations of the three cases given in Table 4.4. These plots indicate the normalized vertical flow across the porous layer region toward the model organism. The flows have been normalized in such a way that positive flow indicates fluid moving away from the structure, while negative flow indicates flow moving toward the structure.

flow fields at the end of the expansion phase after one pulse cycle and four pulse cycles generated using is shown in Figure 4.4.

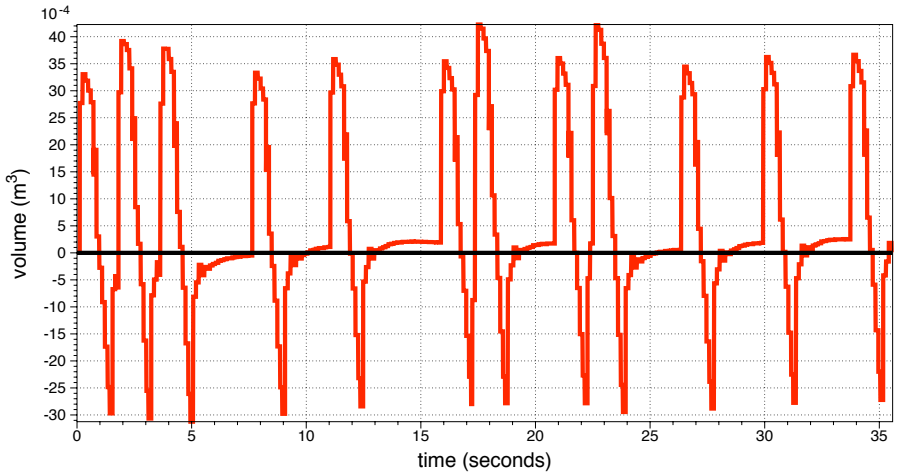

FIGURE 4.3. HFR from the left side of the bell. Volumetric flow rates along the LHFL describing vertical flow moving toward the bell from the left were compared among simulations of the three cases given in Table 4.4. These plots indicate the normalized horizontal flow from the left toward the model organism. The flows have been normalized in such a way so that positive flow indicates fluid moving toward the structure, while negative flow indicates flow moving away from structure.

The HFR and VFR were calculated in the same way as in previous chapters (see Figure 3.2 for the general structure of the flow during a cycle.) For the HFRs the large increase in flow toward the bell corresponded to the beginning of the bell contraction. The decrease of the flow toward the bell occurred during the first pause and the expansion phase. During the second pause (if present), the flow toward the bell continued to decrease and in some cases reversed. For the longer pauses a gradual increase in flow toward the bell and a plateauing of the flow rate was observed before the next contraction begins. For the VFRs, a similar pattern was observed for flow away from the porous layer, a gradual slowing in flow rate and an eventual flow back toward the porous layer, and a gradual slowing in flow toward the porous layer. Fluid was driven through the permeable layer by the motion of the bell. In the absence of a second pause the fluid was advected upwards and away from the jellyfish, as seen by the mixing of the passive tracers.

TABLE 4.4. Sequences of pause times generated using the probabilities associated with Individual 1 from Table 4.1

Pause (s) #	Case 1	Case 2	Case 3
1	0.2568	3.2710	2.4114
2	0.4000	2.9198	1.2101
3	2.5763	2.0553	0.3601
4	1.9789	0.3268	1.2626
5	3.4006	0.2500	0.0169
6	0.0529	4.2077	0.2433
7	2.0444	0.1999	0.1250
8	0.2353	0.1921	2.6353
9	2.4276	0.3854	0.0320
10	2.1426	0.1411	0.0974
11	2.3736	0.1971	0.1527
12	0.5328	0.2990	3.2157

For a constant two (2) second pause, mixing occurred around the porous layer. In the case of the DTM process, the pattern alternated between advection up and away from the bell and mixing over the porous layer as seen in Figure 4.4.

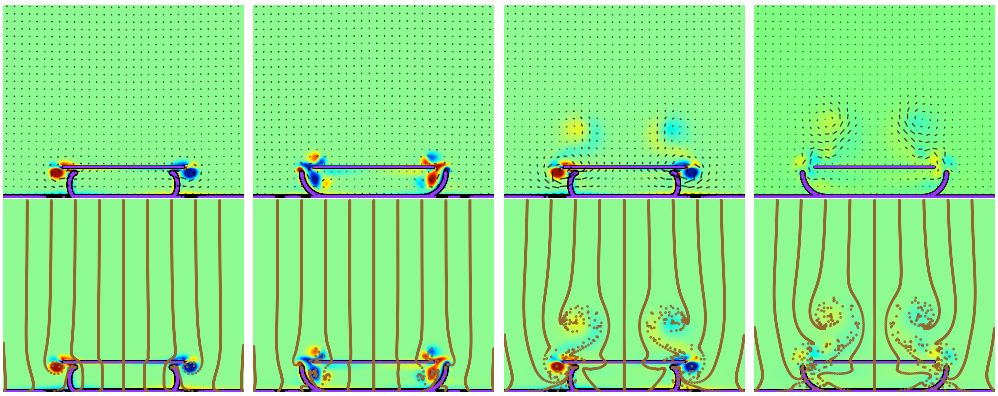

FIGURE 4.4. Vorticity plots for a model following the sequence of pause times shown in Case 1 from Table 4.4 from numerical simulations. Warm colors show regions of positive vorticity while cool colors are areas of negative vorticity. Top, left to right: vorticity plots for the model at the first contraction, the first full cycle, the fourth contraction, and the fourth full cycle with overlain velocity vector fields. The vortices advected upward were shed after two cycles with short pauses. Bottom, left to right: vorticity plots for the model at the first contraction, the first full cycle, the fourth contraction, and the fourth full cycle with tracer particles that move with the local fluid velocity.

TABLE 4.5. Conditions for the two-jellyfish models. Random timing used was Case 3 from Table 4.4

Additional Parameters	Case #
Both with 2.0 s pauses	1B
Left with 2.0 s pauses Right with random timing	2B
Both with same random timing	3B
Both with no pauses	4B
Spaced $L/2$ apart	5B
Spaced $L/8$ apart	6B
Left bell half the size of the right bell	7B

4.4.2. Multiple jellyfish. A summary for the simulations run with the multiple jellyfish models is given in Table 4.5. Flow lines are shown in Figure 4.5. Horizontal flow lines were vertical lines of length 0.07 m. Vertical flow lines were horizontal lines of length 0.0615 m. The left horizontal flow line (LHFL) was $0.4L$ to the left of the outside surface of the bell. The left vertical flow line (LVFL) was drawn on top of the porous layer of the left model. The interior flow line (IFL) was drawn horizontally between the two bells 3 grid cells away from either side of the bells. The right vertical flow line (RVFL) was drawn on top of the porous layer of the right model. The right horizontal flow line (RHFL) was $0.4L$ to the right of the outside surface of the bell. In cases 5B-7B where the position of the bell edges changed, the position of the flow lines was moved in order to maintain the same absolute distance from the bell, but the general area in which each of the flow lines was defined did not change.

4.4.2.1. *Effect of pulse timing.* Vorticity plots for Case 1B (the "basic model" with two identical jellyfish spaced $L/4$ apart and with synchronized 2.0 s pauses) are shown in Figure 4.6. The stronger vorticity structure on the sides of the bell adjacent to one another created an asymmetry in the flow around each porous layer. The stronger vortices

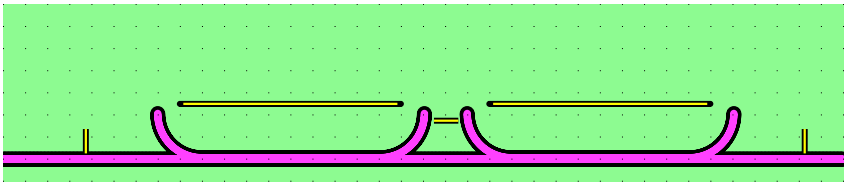

FIGURE 4.5. Positions of the flow lines used to measure the volumetric flow rates around the bell. From left to right the yellow lines are 1) the left horizontal flow line (LHFL) which was $0.4L$ to the left of the outside of the bell; 2) the left vertical flow line (LVFL) which was drawn on top of the porous layer of the left model; 3) the interior flow line (IFL) which was drawn between the two bells 3 grid cells away from either side of the bells; 4) the right vertical flow line (RVFL) which was drawn on top of the porous layer of the right model; 5) the right horizontal flow line (RHFL) which was $0.4L$ to the right of the outside of the bell.

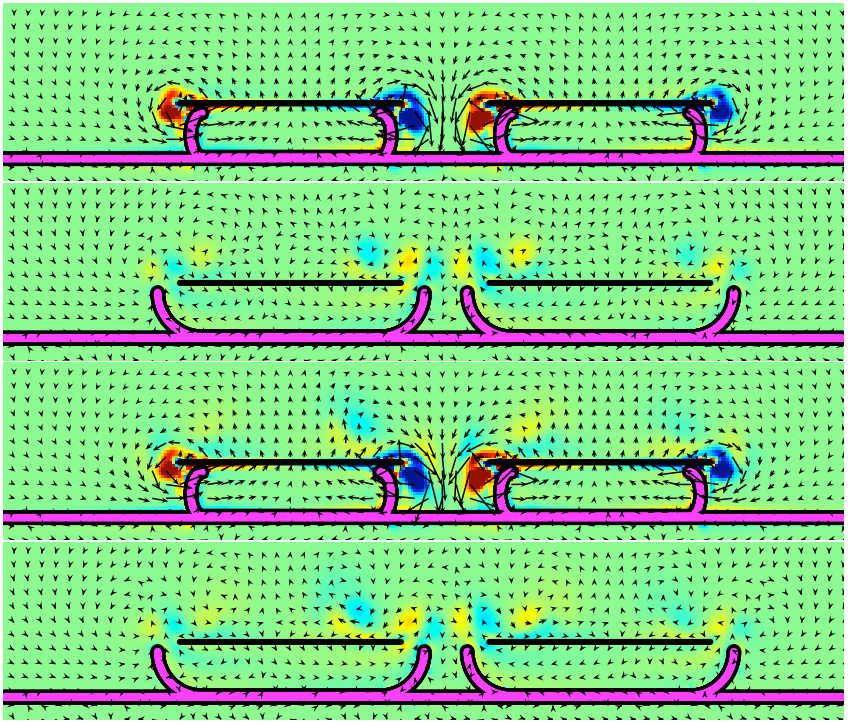

FIGURE 4.6. Vorticity plots for a model following the sequence of pause times shown in Case 1B (two jellyfish spaced $L/4$ apart and with synchronized 2.0 s pauses) from Table 4.5 from numerical simulations. Warm colors show regions of positive vorticity while cool colors are areas of negative vorticity. Top to bottom: vorticity plots for the model at the first contraction, the first full cycle, the fourth contraction, and the fourth full cycle with overlain velocity vector fields.

near the inside bell margins were trapped around their respective porous layers, resulting in an increased area of affected fluid when compared with the vortices of individual organisms.

4.4.2.2. *Effect of pulse timings.* In order to examine the effect of differences in pulse dynamics, simulations for models with synchronized constant pulses (Case 1B), with asynchronous pulses (Case 2B) and with synchronized random pulses (Case 3B) were compared. Comparisons of flow rates in the randomly pulse models in Cases 2B, 3B, and Case 3 (the corresponding individual Markov jellyfish) are given in Figure 4.7. The

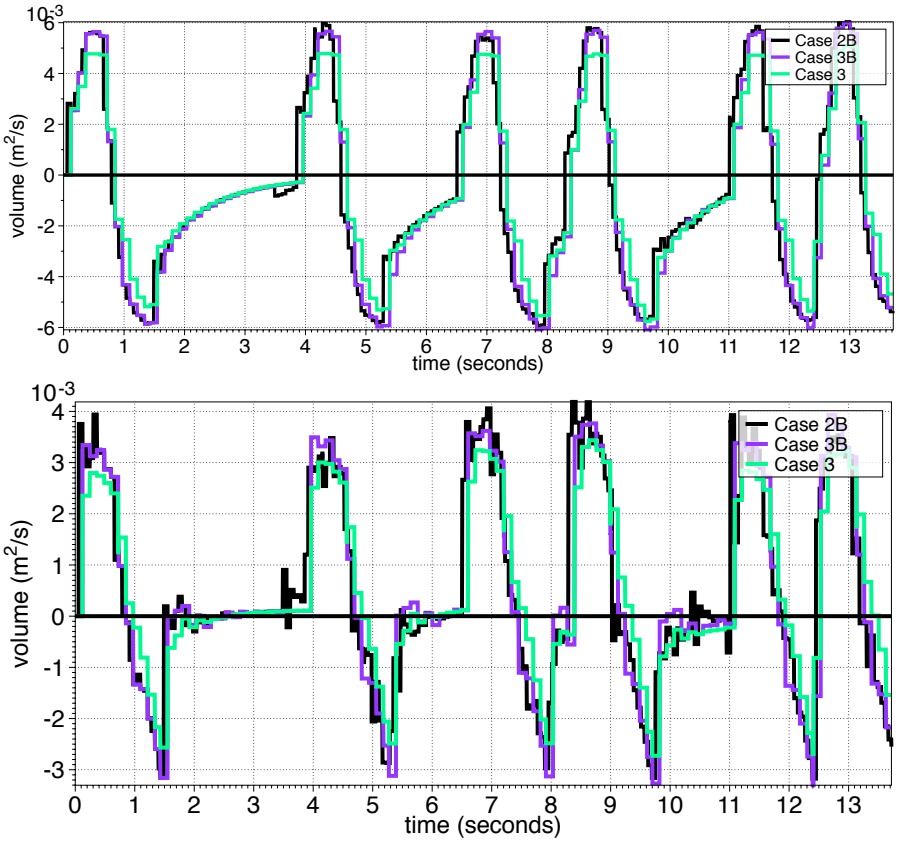

FIGURE 4.7. Volumetric flow rates for Cases 2B, 3B, and 3. The flow rates for two jellyfish with different pauses in Case 2B is shown in black, while the two jellyfish with the same random pauses in Case 3B is shown in purple and the single randomly pulsing jellyfish is shown in bright green.

RHFR and the RVFR for the multiple jellyfish was slightly increased in magnitude compared to the single pulsing jellyfish in Case 3. The RHFR for the model in Case 2B with the asynchronous pulses showed slight fluctuations corresponding to the pulse pattern of the model on the left. A corresponding pattern was seen in the LHFR for Case 2B when compared to a single individual with constant pauses.

4.4.2.3. *Effect of relative spacing.* The LHFR, RHFR, IFR, LVFR, and RVFR are given for cases 1B (basic model with $L/4$ spacing), 5B (spaced $L/2$ apart), and 6B (spaced $L/8$ apart) in Figure 4.8. Vorticity plots at the end of the first contraction are shown in Figure 4.10 to compare the difference in the strength of the interior vortices (the vortices of the individual specimens adjacent to one another.) Vorticity plots for the closest spaced models (Case 6B) are shown in Figure 4.9. The strength of the vortices did not change much between the basic model (Case 1B) and Case 5B (increased spacing), but changed dramatically between the basic model (Case 1B) and Case 6B (decreased spacing). The spacing of the models slightly changed the HFRs on either side of the bells, while it makes virtually no difference to the VFR across each porous layer. The increased spacing of the bells noticeably decreased the IFR, while the close spacing dramatically increased the exchange across the interior flow line (IFL).

4.4.2.4. *Effect of relative size.* To examine the effects of the size of the neighboring model, simulations were performed for a normal model and a small model(half the length and width of the right model) spaced 3L/8 apart (the same distance from the center of the domain relative to body size for each model.) The vortices (Figure 4.11) from the left

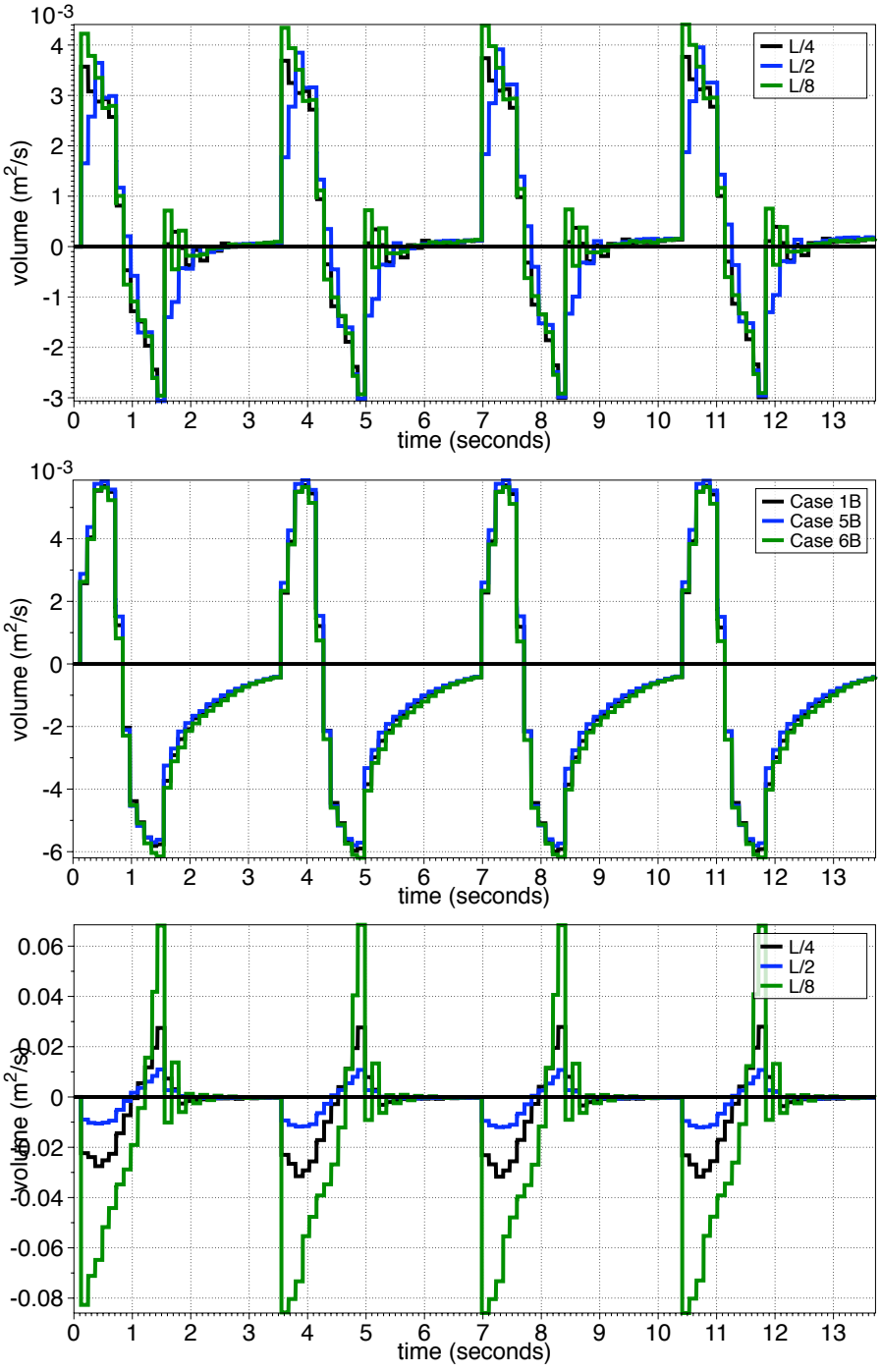

FIGURE 4.8. Volumetric flow rates for Cases 1B, 5B, and 6B. The flow rates for two jellyfish spaced $L/4$ apart are shown in black in each subfigure, while the flow rates for jellyfish spaced $L/2$ apart are shown in blue and the jellyfish spaced $L/8$ apart is shown in green.

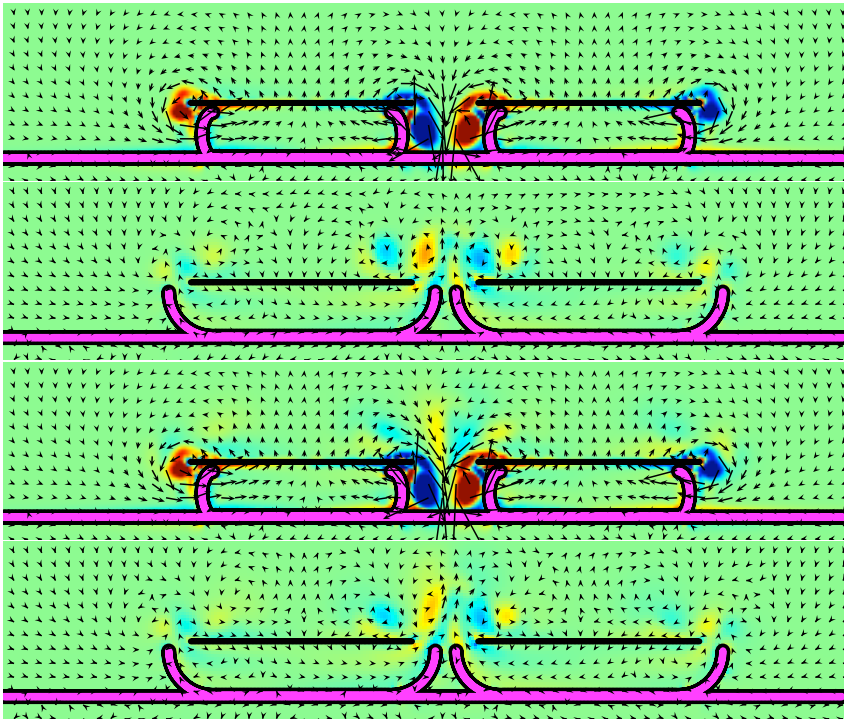

FIGURE 4.9. Vorticity plots for a model following the sequence of pause times shown in Case 6B from Table 4.5 from numerical simulations. Warm colors show regions of positive vorticity while cool colors are areas of negative vorticity. Top to bottom: vorticity plots for the model at the first contraction, the first full cycle, the fourth contraction, and the fourth full cycle with overlain velocity vector fields.

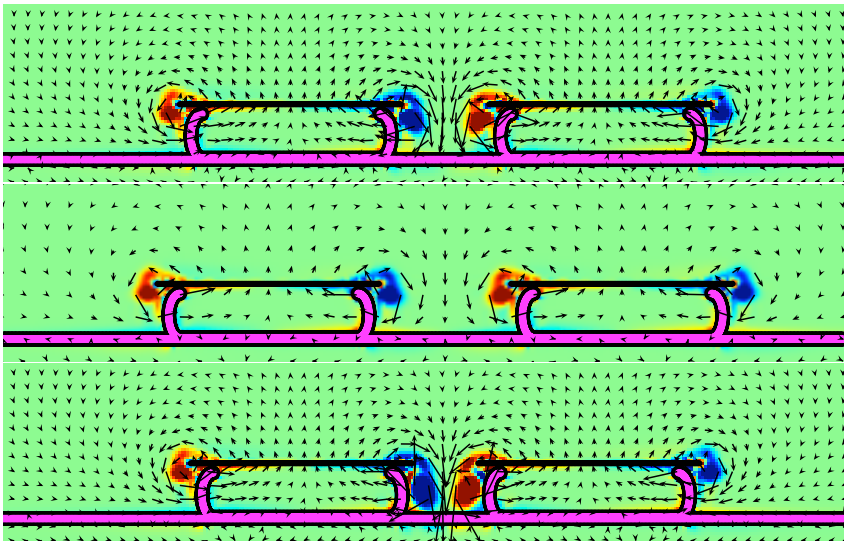

FIGURE 4.10. Vorticity plots for three models simulating the interaction of multiple jellyfish spaced different distances apart. Top: spacing was L/4, Middle: spacing was L/2, Bottom: spacing was L/8.

margin of the larger bell draws fluid strongly back and forth across the region above the porous layer of the smaller bell on the left. The comparative flow rates are shown in Figure 4.12. The LVFR for the smaller jellyfish is not substantially affected by

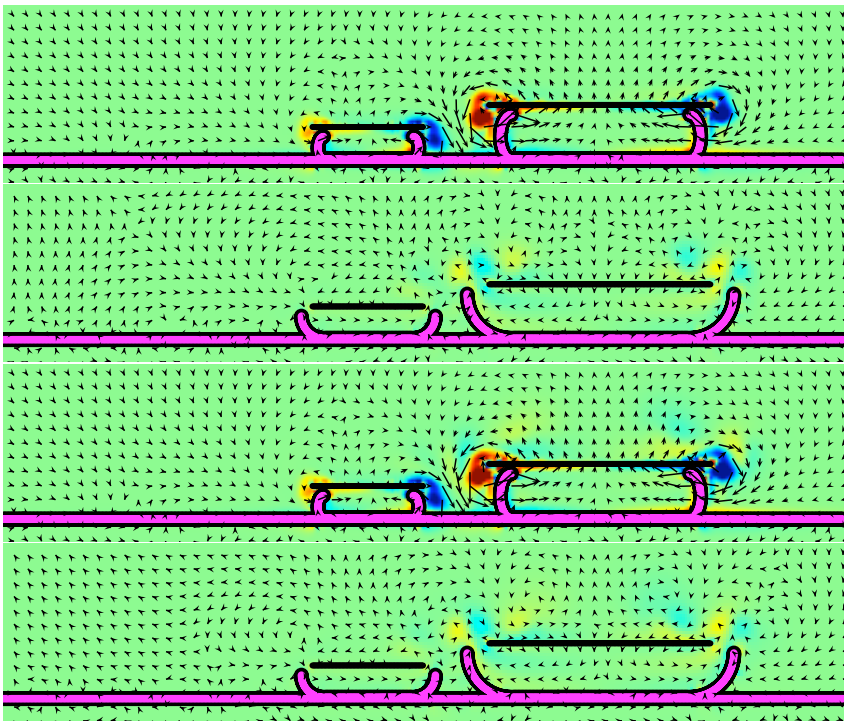

FIGURE 4.11. Vorticity plots for a model following the sequence of pause times shown in Case 7B from Table 4.5 from numerical simulations. Warm colors show regions of positive vorticity while cool colors are areas of negative vorticity. Top to bottom: vorticity plots for the model at the first contraction, the first full cycle, the fourth contraction, and the fourth full cycle with overlain velocity vector fields.

the presence of the larger jellyfish on the right. The LHFR is increased when the large jellyfish is present on the right. Also the IFR is tripled when the larger jellyfish is present. The flow rates for the larger jellyfish are not noticeably affected by the presence of the smaller jellyfish.

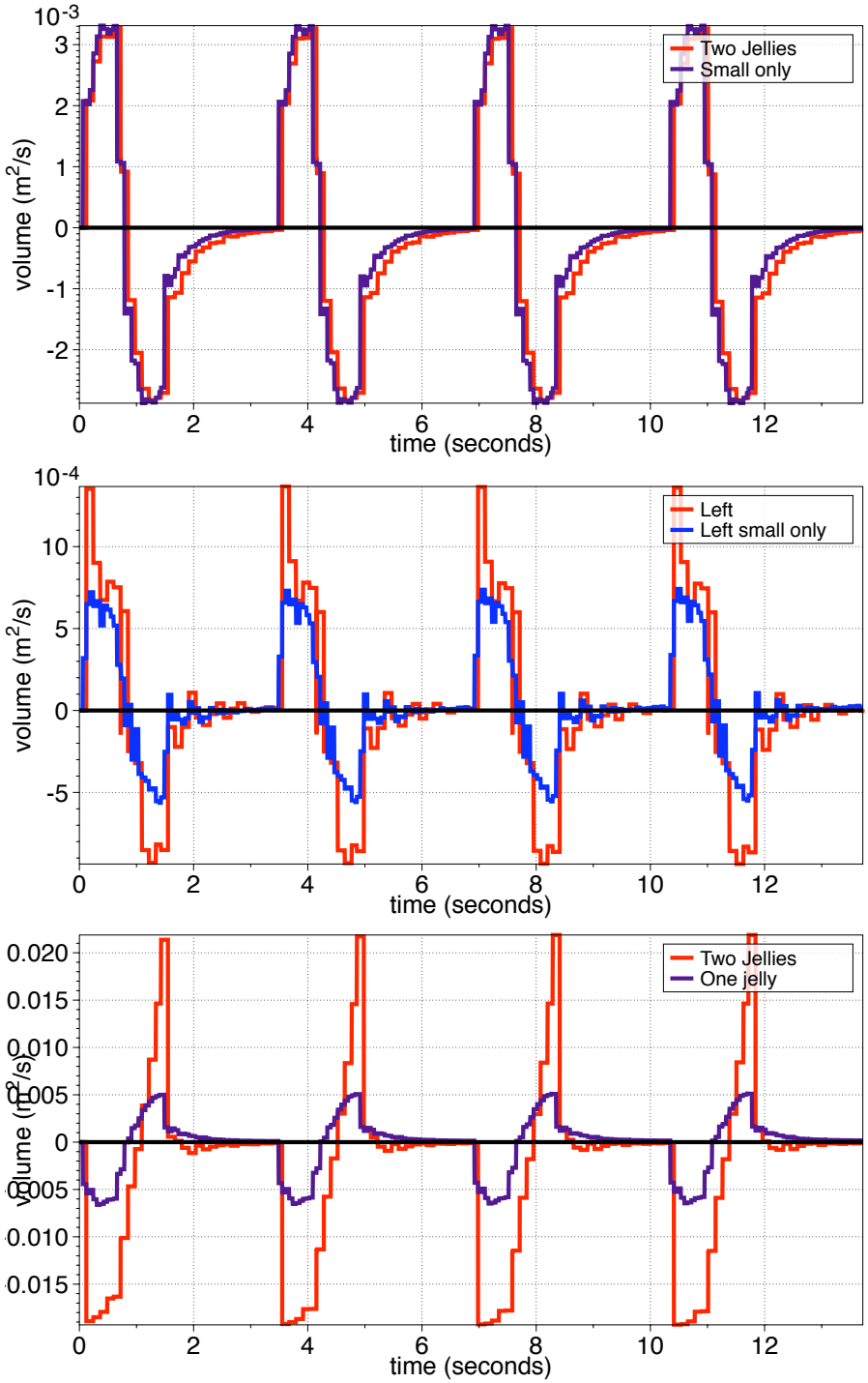

FIGURE 4.12. Volumetric flow rates for a smaller individual jellyfish and a smaller and larger jellyfish side by side. Top: The VFR across the oral arms of the smaller jellyfish on the left is shown. Middle: The LHFR of fluid coming toward the left of the smaller jellyfish is shown. Bottom: The IFR in the area that would be between the two jellyfish is shown for the case of two jellyfish present and the case in which there was only one jellyfish.

4.5. Discussion

This study has shown that both the pulsing patterns of single jellyfish models and the fluid dynamics of groups of jellyfish models have significant consequences for feeding and mixing. Results from the individual Markov chain models of jellyfish suggest that for promoting mixing and transport the actual pattern of the pulse matters less than the fact that both long and short pauses were present. This suggests a fairly robust pattern of mixing and advection that is not sensitive to carefully coordinated patterns. In the case of multiple jellyfish more closely spaced models appear to generate stronger vortices in the region between the bells than models spaced further apart. Such a phenomenon could be advantageous in cases where a number of organisms have grouped together in an effort to sample a region of sparsely distributed resources. Finally it was seen that the flow rates of smaller jellyfish were affected by the pulsing larger jellyfish in a way that draws more fluid across the bell of the smaller organism. This could be advantageous to weakened jellyfish whose bells have shrunk by allowing the small organism to sample the region of flow near a larger organism without disturbing the flow around the larger organism substantially.

In the single Markov model in each of the cases, the jellyfish mix fluid during the long pauses and then advect the fluid upward during the short pauses as seen in Figure 4.4. This could be beneficial for particle exchange and also for ejecting fluid once it has been filtered. This could also aid in the distribution of gametes if there is a low current just above the boundary layer. From the flow rates in Figures 4.2 and 4.3 it was apparent that the change in pauses does not dramatically affect the HFRs or the VFRs in each case.

The LHFR and the RHFR in each of the multiple jellyfish cases except in Case 7B (the different sized jellyfish) does not change appreciably among the simulations tested. It should be noted that other parameter not explored here will be part of future work and will be discussed in the following chapter. In comparing the horizontal and vertical flow rates of two synchronized jellyfish (Case 2B) and two asynchronous jellyfish (Case 3B) with those of Case 3 from the individual Markov jellyfish (see Figure 4.7), it appears that each of the flow rates was slightly enhanced by the presence of the second jellyfish.

The flow in Case 6B (the models spaced L/8 apart) shows more backflow during the relaxation than either Case 1B or Case 5B (spacing L/4 and L/2, respectively), so it appears that closer jellyfish benefit from fluid being pulled toward the bell region. Small fluctuations occur in each flow rate in Case 2B (in which the right model pulses randomly). This suggests that the flow fields were affected by both bells during pulse cycles and indicates that there is synergy if jellyfish are close to one another. The IFR between the bells in the case of the close jellyfish was much more pronounced. This was also apparent from the much stronger vorticity illustrated in Figure 4.9. This phenomenon shows that closer spacing has the potential to draw more particles up from the substrate for sampling. This suggests that in regions where nutrients are scarce it may be beneficial for jellyfish to group together.

The VFR do not change appreciably among the cases except when one of the models was smaller (Case 7B.) In this case, it was likely that most of the change on the left was due to the size of the jellyfish and not as much the presence of the other larger jellyfish. The IFRs (figure 4.18) show that pause timing and even size have little effect on the flow rate in the region between the two bells. The direction of the flow in Case 7B was altered

however (Figure 4.11.) This change in flow direction shows the motion of the right bell drawing fluid down and to the right across the porous layer of the smaller jellyfish during contraction and ejecting fluid up and to the left across the porous layer of the smaller jellyfish during relaxation. The smaller model experiences a larger flow on the right side than the left based on Figure 4.11. In the laboratory injured or sick jellyfish whose bells have shrunk considerably are observed to situate themselves near larger jellyfish. The flow rates and vortices observed in Figures 4.11 and 4.12 indicate that by placing themselves near larger specimens, the smaller specimens may reduce the energy that must be expended to sample a given amount of fluid. This would be beneficial to the smaller organism.

CHAPTER 5

Conclusions, Limitations and Future Directions

5.1. Conclusions

A model of *Cassiopea* has been developed and implemented in computational experiments in an immersed boundary framework. The objectives of these computational studies were to examine the effect of secondary structures on the bulk transport of fluid around the model organism and also to use the developed model to perform experiments across and beyond the limits of the biology of the organism. This type of parameter testing and model manipulation is useful not only in testing the physical constraints on biological systems but also for bio-inspired for engineering design. [**21, 39**]

In Chapter 2, it was shown that the presence of secondary structures with properties such as permeability significantly alter the fluid flow around the main body of the model organism. These results were compared to PIV data from laboratory specimens. The computational simulations containing the porous layer simulating the oral arms and laboratory experiments from the specimens qualitatively agree, suggesting that the flow patterns generated by *Cassiopea* are closely tied to the presence of its oral arm structures. The flow structures from the models without a porous layer or with a nonporous layer did not agree as well with observed flow patterns, indicating also that the consideration of the effect of the oral arms is important to more accurately simulate fluid flow around the organism. In contrast to the impermeable model the porous layer model promotes mixing in and around the feeding region rather than ejecting the fluid up and outward from the bell. The porous layer also induces a continuous flow from the substrate to the bell in contrast to the erratic pattern in the impermeable model.

In Chapter 3, computational experiments were performed to examine the effects of environmental factors such as ambient flow. Unidirectional constant flow, unidirectional

variable flow and bi-directional variable flow through a channel were considered. It was found that the porous layer structure tended to maintain a constant pattern of flow across and through the oral arm region, promoting a consistent pattern of sampling in a wide range of flow regimes. The flows in the cases of models with no oral arms varied significantly. These results suggest that although there may be instances in which the lack of a prominent secondary structure may promote more flow toward the oral arms, the presence of a large oral arm mass helps to maintain feeding and sampling rates even as the ambient flow changes. These results also show that adding secondary structures into the numerical models in many cases significantly changes the character of the fluid flow.

In Chapter 4 the effect of other model organisms in close proximity is examined. Random lengths of pauses in individual model organisms did not affect the flow toward the bell of the model, but they did affect whether the fluid was advected upward, downward, or across the oral arm region. This indicates that changes in pause patterns affect how the fluid moves through the oral arms even through fluid movement along the substrate and toward the bell is unaffected. In the case of neighboring jellyfish models it was shown that having more than one jellyfish side by side enhances the flow rates toward the bell. Closer spacing resulted in a stronger flow between the model organisms, indicating that grouping of organisms might serve to draw more particles up from the substrate, so that the interaction of the bell motions may outweigh competition from surrounding organisms for food. Smaller models in close proximity to larger models benefit from the pulse of the larger model by the increased flow back and forth across the smaller bell's porous layer. This benefit occurs without a significant effect on the flow rates around the larger

bell. This could explain why smaller or shrinking laboratory specimens are observed to nestle close to larger organisms inside the aquaria.

5.2. Limitations and future directions

A model that captures some of the fundamental qualitative patterns in the bulk flow of fluid and immersed particles across the bell of the upside-down jellyfish has been developed. By comparing the modeled flow patterns to experimental PIV data it is shown that the flow field generated by the organism is similar in character to the results from numerical computations. Rather than attempting to match the morphology of the organism exactly, important aspects of each structure have been represented by simple mathematical models that capture fundamental aspects of the structure. This simplification allows for larger parameter sweeps to explore the effects of morphology, scale, and kinematics on bulk fluid flow. It is important to note, however, that these simplified models are not intended to replace detailed three-dimensional simulations that provide valuable insight into the physics of specific cases. A three-dimensional model incorporating more detail associated with the secondary structures would be desirable. in order to more accurately capture the effect of the porous structure. In addition more complex ambient flow patterns and arrangement of neighboring model organisms would further enhance our understanding of the system.

In many cases analysis of the vorticity plots combined with the volumetric flow rates around the bell revealed patterns in the bulk flow of fluid. This technique however was not always able to capture some of the mixing observed in the simulations in a precise way. The introduction of particles as in Chapter 2 facilitated the tracking of mixing patterns. The method used in Chapter 2 is difficult to implement in channel

flow simulations due to the strong advection of particles in the middle of the channel. In the future, implementation of finite time Lyaponouv exponents and the analysis of Lagrangian coherent structures similar to the work found in [**59, 61**] will provide a more accurate picture of the mixing behavior.

The preferred motion of the target points is a step away from fully prescribed motion in that the interactions between the generated forces along the boundary and the fluid determine the actual motion of the structure. However target point-driven motion still falls short of the more desirable goal to couple the fluid motion to deformation due to muscle contraction driving the viscoelastic bell. In particular instead of modeling the motion from the perspective of a muscle contraction generating forces stored as elastic energy inside the mesoglea and a subsequent release of that energy during the relaxation of the material, this model relies on timing the bell from observations of video footage. In order to develop a fully coupled system, the next steps would be to develop models of muscle driven forces and to couple these forces to the viscoelastic material that constitutes most of the organism.

In summary a computational model of a sessile jellyfish was developed to examine the effect of bell pulses on the surrounding fluid. A porous boundary was used to study how incorporating secondary structures affects the performance of the bell motion in terms of the resulting flow patterns that promote fluid sampling and feeding. The results here indicate some of the roles prominent secondary structures might play in enhancing feeding from the surrounding fluid in a relatively sessile organism and offer insights for designs that could be incorporated into engineering designs for vehicles for particle sampling for filtration or generation of bio-energy. While three dimensional models and

more accurate structural properties would be required to fully capture the behavior of the entire system, the work presented here provides information about the importance of incorporating additional structures into simplified systems in order to describe the complex mechanisms at work in biological systems.

APPENDIX A

Discretization of equations in the Immersed Boundary Method

Discretization details of the version of the immersed boundary method used in this work are given here. For a more complete treatment of the methods used here, see [**41**], [**64**] and [**62**]. The system of immersed boundary equations are given in the main text, but are repeated here for convenience and clarity.

to discretize the Navier-Stokes equations for incompressible fluids given by

$$\rho\left[\frac{\partial \mathbf{u}(\mathbf{x},t)}{\partial t}+\mathbf{u}(\mathbf{x},t)\cdot\nabla\mathbf{u}(\mathbf{x},t)\right]=-\nabla p(\mathbf{x},t)+\mu\nabla^{2}\mathbf{u}(\mathbf{x},t)+\mathbf{f}(\mathbf{x},t)+\mathbf{f}_{ext} \tag{A.1}$$

$$\nabla\cdot\mathbf{u}(\mathbf{x},t)=0 \tag{A.2}$$

$$\mathbf{F}(\mathbf{X}(s,t),t)=k(\mathbf{X}(s,t)-\mathbf{Y}(s,t)) \tag{A.3}$$

$$\mathbf{f}(\mathbf{x},t)=\int\mathbf{F}(\mathbf{X}(s,t),t)\,\delta(\mathbf{x}-\mathbf{X}(s,t))\,ds \tag{A.4}$$

$$\mathbf{f}_{ext}=-k_{R}(\mathbf{u}_{t}(\mathbf{x},t)-\mathbf{u}(\mathbf{x},t)) \tag{A.5}$$

$$\frac{\partial \mathbf{X}}{\partial t} = \mathbf{U}\left(\mathbf{X}\left(s,t\right)\right) = \int \mathbf{u}\left(\mathbf{x},t\right)\delta\left(\mathbf{x}-\mathbf{X}\left(s,t\right)\right)d\mathbf{x} \tag{A.6}$$

$$\delta_h\left(\mathbf{x}\right) = \frac{1}{h^2}\phi\left(\frac{x}{h}\right)\phi\left(\frac{y}{h}\right) \tag{A.7}$$

where

$$\phi\left(r\right) = \begin{cases} \frac{1}{4}\left(1+\cos\left(\frac{\pi r}{2}\right)\right) & |r| \leq 2 \\ 0 & \text{otherwise} \end{cases} \tag{A.8}$$

let Δt be the time step, Δs be the boundary step at the beginning of the simulation, s be the index of the boundary points, and h be the spatial step on the Cartesian grid. The system given above was solved on a fixed 512x512 square Cartesian grid with periodic boundary conditions. The ∇ operator is discretized in two dimensions by $\left(\mathbf{D}^0\phi\right) = \left(D_1^0, D_2^0\right)$ where

$$\left(D_\alpha^0\right)\left(\mathbf{x}\right) = \frac{\phi\left(\mathbf{x}+h\mathbf{e}_\alpha\right)-\phi\left(\mathbf{x}-h\mathbf{e}_\alpha\right)}{2h}. \tag{A.9}$$

The partial derivative $\partial/\partial x_\alpha$ is discretized by

$$\left(D_\alpha^+\phi\right)\left(\mathbf{x}\right) = \frac{\phi\left(\mathbf{x}+h\mathbf{e}_\alpha\right)-\phi\left(\mathbf{x}\right)}{h} \tag{A.10}$$

$$\left(D_\alpha^-\phi\right)\left(\mathbf{x}\right) = \frac{\phi\left(\mathbf{x}\right)-\phi\left(\mathbf{x}-h\mathbf{e}_\alpha\right)}{h} \tag{A.11}$$

where D_α^+ and D_α^- are forward and backward differencing schemes, respectively. The Laplacian operator Δ is discretized by $\sum_{\alpha=1}^{2} D_\alpha^+ D_\alpha^-$.

To treat the nonlinear term in the Navier-Stokes equations, a skew symmetric difference operator is defined by

$$S_h(u)\,\phi = \frac{1}{2}\mathbf{u}\cdot\mathbf{D}_h^0\phi + \frac{1}{2}\mathbf{D}_h^0\cdot(\mathbf{u}\phi). \tag{A.12}$$

Using these schemes and an implicit-explicit time discretization, the full discretization of the Navier-Stokes equations become

$$\rho\left(\frac{\mathbf{u}^{n+1}-\mathbf{u}^{n+1}}{\Delta t} + S_h(\mathbf{u}^n)\,\mathbf{u}^n\right) + \mathbf{D}_h^0 p^{n+1} = \mu\sum_{\alpha=1}^{2} D_\alpha^+ D_\alpha^- \mathbf{u}^{n+1} + \mathbf{f}^n + \mathbf{f}_{ext}^n. \tag{A.13}$$

The interaction equations (Equations A.4 and A.6) are discretized as sums indexed over the set of boundary points denoted by s and over the set of Cartesian points denoted by x, respectively.

$$\mathbf{f}^n(\mathbf{x}) = \sum_s \mathbf{F}^n((s),t)\,\delta_h(\mathbf{x}-\mathbf{X}^n(s))\,\Delta s \tag{A.14}$$

$$\mathbf{U}^{n+1}(s) = \sum_x \mathbf{u}^{n+1}(\mathbf{x})\,\delta_h(\mathbf{x}-\mathbf{X}^n(s))\,h^2 \tag{A.15}$$

The boundary points are then moved at the local fluid velocity by

$$\mathbf{X}^{n+1}(s) = \mathbf{U}^{n+1} + \Delta t\mathbf{X}^n(s) \tag{A.16}$$

and the porosity of the permeable layer is incorporated using the equation

$$\mathbf{X}_2^{n+1}(s) = \mathbf{U}_2^{n+1} + \Delta t\mathbf{X}_2^n(s) + \lambda\mathbf{F}_2^n \tag{A.17}$$

where the index 2 denotes the second component (the y-direction) of the respective vectors.

The resulting fluid equations are linear in the unknowns $\mathbf{u}^{n+1}$ and p^{n+1}. Because of the linearity of the unknowns and the periodicity of the boundary conditions, the Fast Fourier transform technique was chosen as an appropriate solution method with relatively low computational cost. See [**63**] for details of the Fast Fourier Transform method. The software package FFTW (Massachusetts Institute of Technology, Cambridge, MA) was used to execute the transforms in the simulations.

BIBLIOGRAPHY

1. R. J. Adrian, *Particle imaging techniques for experimental fluid mechanics*, Ann. Rev. Fl. Mech. **23** (1991), 261–304.

2. R. M. Alexander, *Viscoelastic properties of the body-wall of sea anemones*, J. Exp. Biol. **39** (1962), no. 3, 373–386.

3. _____, *Viscoelastic properties of the mesogloea of jellyfish*, J. Exp. Biol. **41** (1964), no. 2, 363–369.

4. A. Andersen, U. Pesavento, and Z.J. Wang, *Analysis of transitions between fluttering, tumbling and steady descent of falling cards.*, J. Fluid Mech. **541** (2005), 91–104.

5. M.N. Arai, *Functional biology of Scyphozoa*, 1st ed., New York: Springer, 1996.

6. R. D. Bartleson, *Interations of seagrass beds and the water column: Effects of bed size and hydrodynamics*, Ph.D. thesis, University of Maryland, College Park, 2004.

7. J. T. Beale and A. T. Layton, *A velocity decomposition approach for moving interfaces in viscous fluids*, J. Comput. Phys. **228** (2009), 3358–3367.

8. R. P. Bigelow, *The anatomy and development of* Cassiopea xamachana, Boston Soc. Nat. Hist. Mem. **5** (1900), 191–236.

9. D. C. Bottino, *Modeling viscoelastic networks and cell deformation in the context of the immersed boundary method*, J. Comput. Phys. **147** (1998), no. 1, 86 – 113.

10. R.C. Brusca and G.J. Brusca, *Invertebrates*, 2nd ed., Sunderland, Mass.: Sinauer Associates, 2003.

11. S. P. Colin and J. H. Costello, *In situ swimming and feeding behavior of eight co-occurring hydromedusae*, Mar. Ecol. Prog. Ser. **253** (2003), 305–309.

12. J. H. Costello and S. P. Colin, *Prey resource use by coexistent hydromedusae from Friday Harbor, Washington*, Limnol. Oceanogr. **47** (2002), no. 4, 934–942.

13. J. O. Dabiri, *On the estimation of swimming and flying forces from wake measurements*, J. Exp. Biol. **208** (2005), no. 18, 3519–3532.

14. _____, *Optimal vortex formation as a unifying principle in biological propulsion*, Ann. Rev. Fl. Mech. **41** (2008), 17–33.

15. J. O. Dabiri, S. P. Colin, and J. H. Costello, *Morphological diversity of medusan lineages constrained by animal-fluid interactions*, J. Exp. Biol. **210** (2007), 1868–1873.

16. J. O. Dabiri, S. P. Colin, and K. Katija, *A wake-based correlate of swimming performance and foraging behavior in seven co-occurring jellyfish species.*, J. Exp. Biol. **213** (2010), 1217–1225.

17. T. L. Daniel, *Cost of locomotion: Unsteady medusan swimming*, J. Exp. Biol. **119** (1985), no. 1, 149–164.

18. T. L. Daniel and M. S. Tu, *Animal movement, mechanical tuning and coupled systems*, J. Exp. Biol. **202** (1999), 3415–3421.

19. M. E. Demont and J. M. Gosline, *Mechanics of jet propulsion in the hydromedusan jellyfish,* Polyorchis pexicillatus*: II. B energetics of the jet cycle*, J. Exp. Biol. **134** (1988), 333–345.

20. _____, *Mechanics of jet propulsion in the hydromedusan jellyfish,* Polyorchis pexicillatus*: III. A natural resonating bell; the presence and importance of a resonant phenomenon in the locomotor structure*, J. Exp. Biol. **134** (1988), no. 1, 347–361.

21. M. H. Dickinson, R. J. Farley, M.A.R. Koehl, R. Kram, and S. Lehman, *How animals move: An integrative view*, Science **288** (2000), 100–106.

22. R. H. Dillon, L. J. Fauci, A. Fogelson, and D. Gaver, *Modeling biofilm processes using the immersed boundary method*, J. Comput. Phys. **129** (1996), no. 1, 57–73.

23. R. H. Dillon, L. J. Fauci, C. Omoto, and X. Yang, *Fluid dynamic models of flagellar and ciliary beating*, Ann. N. Y. Acad. Sci. **1101** (2007), 494–505.

24. R. H. Dillon, L. J. Fauci, and X. Yang, *Sperm motility and multiciliary beating: An integrative mechanical model*, Comput. Math. Appl. **52** (2006), no. 5, 749–758.

25. P. B. Dobrin, *Mechanical properties of arteries*, Physiol. Rev. **58** (1978), no. 2, 397–460.

26. L. J. Fauci and A. L. Fogelson, *Truncated Newton methods and the modeling of complex immersed elastic structures*, Comm. Pure and Appl. Math. **46** (1993), 787–818.

27. L. J. Fauci and A. McDonald, *Sperm motility in the presence of boundaries*, Bull. Math. Bio. **57** (1995), 679–699.

28. L. J. Fauci and C. S. Peskin, *A computational model of aquatic and animal locomotion*, J. Comput. Phys. **77** (1988), no. 85-108.

29. W. K. Fitt and K. Costley, *The role of temperature in survival of the polyp stage of the tropical rhizostome jellyfish* Cassiopea xamachana, J. Exp. Mar. Bio. and Eco. **222** (1998), 79–91.

30. A. L. Fogelson and R. D. Guy, *Immersed-boundary-type models of intravascular platelet aggregation*, Comp. Meth. Appl. Mech. Eng. **197** (2008), no. 25-28, 2087 – 2104.

31. B.E. Griffith, X. Luo, D.M. McQueen, and C.S. Peskin, *Simulating the fluid dynamics of natural and prosthetic heart valves using the immersed boundary method*, Int. J. Appl. Mech. **1** (2009), 137–177.

32. C. M. Grinstead and J. L. Snell, *Introduction to probability*, 2nd revised ed., American Mathematical Society, Providence, RI, 1997.

33. C. L. Hamlet, A. Santanakrishnan, and L. A. Miller, *A numerical study of the effects of bell pulsation dynamics and oral arms on the exchange currents generated by the upside-down jellyfish* Cassiopea *sp.*, J. Exp. Biol. (In press).

34. K. Hasselmann, T.P. Barnett, E. Bouws, H. Carlson, D.E. Cartwright, K. Enke, J.A. Ewing, H. Gienapp, D.E. Hasselmann, P. Kruseman, A. Meerburg, P. Mller, D.J. Olbers, K. Richter, W. Sell, and H. Walden, *Measurements of wind-wave growth and swell decay during the joint north sea wave project (jonswap)*, Ergnzungsheft zur Deutschen Hydrographischen Zeitschrift Reihe, A **8** (1973), no. 12, 95.

35. T. Y. Hou and Z. Shi, *An efficient semi-implicit immersed boundary method for the Navier-Stokes equations*, J. Comput. Phys. **227** (2008), 8968–8969.

36. L. H. Hyman, *The invertebrates*, vol. 1. Protozoa through Ctenophora, New York: McGraw-Hill, 1940 (English).

37. D. Ito, E. Tanaka, and S. Yamamoto, *A novel constitutive model of skeletal muscle taking into account anisotropic damage*, J. Mech. Behav. Biomed. **3** (2010), no. 1, 85–93.

38. C. Jantzen, C. Wild, M. Rasheed, M. El-Zibdah, and C. Richter, *Enhanced pore-water nutrient fluxes by the upside-down jellyfish* Cassiopea sp. *in a red sea coral reef*, Mar. Ecol. Prog. Ser. **411** (2010), 117–125.

39. A. Jusufi, I. Daniel, S. R. Goldman, and R. J. Full, *Active tails enhance aboreal acrobatics in geckos.*, Proc. Natl. Acad. Sci. **105** (2008), no. 11, 4215–4219.

40. Y. Kim, M. C. Lai, and C. S. Peskin, *Numerical simulations of two-dimensional foam by the immersed boundary method*, J. Comput. Phys. **229** (2010), no. 13, 5194–5207.

41. Y. Kim and C. S. Peskin, *2-D parachute simulation by the immersed boundary method*, SIAM J. Sci. Comput. **28** (2006), no. 6, 2294–2312.

42. D. Kobashi and Y. Mazda, *Tidal flow in riverine-type mangroves*, Wetlands Ecology and Management **13** (2005), 615–619.

43. M.A.R. Koehl, *Mechanical diversity of connective tissue of the body wall of sea anemones*, J. Exp. Biol. **69** (1977), no. 1, 107–125.

44. _____, *How do benthic organisms withstand bending water?*, Amer. Zool. **24** (1984), 57–70.

45. Moskowitz L., *Estimates of the power spectrums for fully developed seas for wind speeds of 20 to 40 knots*, Journal of Geophysical Research **69** (1964), no. 24, 5161–5179.

46. R. Lewandowski and B. Chorazyczewski, *Identification of the parameters of the Kelvin-Voigt and the Maxwell fractional models, used in modeling of viscoelastic dampers*, Comput. Struct. **88** (2010), no. 1-2, 1–17.

47. D. Lipinski and K. Mohseni, *Flow structures and fluid transport for the hydromedusae* Sarsia tubulosa *and* Aequora victoria, J. Exp. Biol. **212** (2009), 2436–2447.

48. _____, *A ridge tracking algorithm and error estimate for efficient computation of Lagrangian coherent structures*, Chaos **20** (2010), no. 1, 017504–1–017504–9).

49. S. Lukens, X. Yang, and L. Fauci, *Using Lagrangian coherent structures to analyze fluid mixing by cilia*, Chaos **20** (2010), no. 1, 017511–1–017511–8.

50. H. Luo, R. Mittal, X. Zheng, S. A. Bielamowicz, R. J. Walsh, and J. K. Hahn, *An immersed-boundary method for flow–structure interaction in biological systems with application to phonation*, J. Comput. Phys. (Accepted).

51. C. Macosko, *Rheology: Principles, measurements and applications*, John Wiley and Sons Inc., 1994.

52. Y. Mazda, E. Wolanski, B. King, A. Sase, D. Ohtsuka, and M. Magi, *Drag force due to vegetation in mangrove swamps*, Mangroves and Salt Marshes **1** (1997), 193–199.

53. L. A. Miller and C. S. Peskin, *Flexible clap and fling in tiny insect flight*, J. Exp. Biol. **212** (2009), no. 19, 3076–3090.

54. R. Mittal and G. Iaccarino, *Immersed boundary methods*, Ann. Rev. Fl. Mech. **37** (2005), 239–261 (English).

55. F. A. Morrison, *Understanding rheology*, Oxford University Press, 2001.

56. E. P. Newren, A. L. Fogelson, R. D. Guy, and R. M. Kirby, *Unconditionally stable discretizations of the immersed boundary equations*, J. Comput. Phys. **222** (2007), 702–719.

57. W. Niggl and C. Wild, *Spatial distribution of the upside-down jellyfish* Cassiopea sp., Helgol. Mar. Res. **64** (2010), 281–287.

58. T. Peacock and J. Dabiri, *Introduction to focus issue: Lagrangian coherent structures*, Chaos **20** (2010), no. 1, 017501–1–017501–3.

59. J. Peng and J. O. Dabiri, *An overview of a Lagrangian method for analysis of animal wake dynamics*, J. Exp. Biol. **211** (2008), 280–287.

60. _____, *The 'upstream wake' of swimming and flying animals and its correlation with propulsive efficiency*, J. Exp. Biol. **211** (2008), no. 16, 2669–2677.

61. _____, *Transport of inertial particles by lagrangian coherent structures: application to predator-prey interaction in jellyfish feeding*, J. Fluid Mech. **623** (2009), 75–84.

62. C. S. Peskin, *The immersed boundary method*, Acta Numer. **11** (2002), 479–517. MR 2009378 (2004h:74029)

63. C. S. Peskin and McQueen D.M., *Fluid dynamics of the heart and its valves In: Case studies in mathematical modeling: Ecology, physiology, and cell biology*, 2nd ed., Prentice-Hall, 1996.

64. C. S. Peskin and B. F. Printz, *Improved volume conservation in the computation of flows with immersed elastic boundaries*, J. Comput. Phys. **105** (1993), 33–46.

65. Boris Rubinstein, Maxime F. Fournier, Ken Jacobson, Alexander B. Verkhovsky, and Alex Mogilner, *Actin-myosin viscoelastic flow in the keratocyte lamellipod*, Biophys. J. **97** (2009), no. 7, 1853–63.

66. D. Rudolf, *Animating jellyfish through numerical simulation and symmetry exploitation*, Master's thesis, University of Saskatchewan, 2007.

67. M. Sahin and K. Mohseni, *An arbirtrary Lagrangian-Eulerian formulation for the numerical simulation of flow patterns generated by the hydromedusa* Aequorea victoria, J. Comput. Phys. **228** (2009), 4588–4605.

68. M. Sahin, K. Mohseni, and S. P. Colin, *The numerical comparison of flow patterns and propulsive performances for the hydromedusae* Sarsia tubulosa *and* Aequorea victoria, J. Exp. Biol. **212** (2009), no. 16, 2656–2667.

69. A. Santanakrishnan, N. Nguyen, J. Gunderson, and L. A. Miller, *Flow within models of the vertebrate embryonic heart*, J. Theor. Biol. **259** (2009), no. 3, 449–461.

70. S. C. Shadden, F. Lekien, and J. E. Marsden, *Definition and properties of Lagrangian coherent structures from finite-time Lyapunov exponents in two-dimensional aperiodic flows aperiodic flows*, Physica D: Nonlinear Phenomena **212** (2005), no. 3-4, 271–304.

71. M. J. Sherratt, *Tissue elasticity and the ageing elastic fibre*, Age **31** (2009), no. 4, 305–325.

72. W. Sterrer, *Marine fauna and flora of bermuda: A systematic guide to the identification of marine organisms*, John Wiley and Sons Inc., 1986.

73. J. M. Stockie, *Modelling and simulation of porous immersed boundaries*, Comput. Struct. **87** (2009), no. 11-12, 701–709.

74. J. M. Stockie and S. I. Green, *Simulating the motion of flexible pulp fibres using the immersed boundary method*, J. Comput. Phys. **147** (1998), 147–165.

75. M. A. Templeman and M. J. Kingsford, *Trace element accumulation in* Cassiopea sp. *(Scyphozoa) from urban marine environments in Australia*, Mar. Environ. Res. **69** (2010), no. 2, 63–72.

76. J. Teran, L. Fauci, and M. Shelley, *Viscoelastic fluid response can increase the speed and efficiency of a free swimmer*, Phys. Rev. Lett. **104** (2010), no. 3, 038101.

77. J. M. Teran and C. S. Peskin, *Tether force constraints in Stokes flow by the immersed boundary method on a periodic domain*, SIAM J. Sci. Comput. **31** (2009), no. 5, 3404–3416.

78. E. D. Tytell, C. Hsu, T. L. Williams, A. H. Cohen, and L. J. Fauci, *Interactions between internal forces, body stiffness, and fluid environment in a neuromechanical model of lamprey swimming*, Proc. Natl. Acad. Sci. (In press).

79. J. J. Verduin and J. O. Backhaus, *Dynamics of plant-flow interactions for the seagrass* Amphibolis antarctica*: Field observations and model simulations*, Estuarine, Coastal and Shelf Science **50** (2000), 185–204.

80. J. F. V. Vincent, *Structural biomaterials*, London: Macmillan, 1982 (English).

81. Z.J. Wang, *Vortex shedding and frequency selection in flapping flight*, J. Fluid Mech. **410** (2000), 323–341.

82. P. N. Watton, X. Y. Luo, X. Wang, G. M. Bernacca, P. Molloy, and D. J. Wheatly, *Dynamic modelling of prosthetic chorded mitral valves using the immersed boundary method*, J. Biomech. **40** (2007), 613–626.

83. D. T. Welsh, R. J. K. Dunn, and T. Maeziane, *Oxygen and nutrient dynamics of the upside down jellyfish (*Cassiopea sp.*) and its influence on benthic nutrient exchanges and primary production.*, Hydrobiologia **635** (2009), 351–362.

84. E. J. West, D. T. Welsh, and K. A. Pitt, *Influence of decomposing jellyfish on the sediment oxygen demand and nutrient dynamics.*, Hydrobiologia **616** (2009), 151–160.

85. C. E. Willert and M. Gharib, *Digital particle image velocimetry*, Exp. Fluids **10** (1991), 181–193.

86. M. M. Wilson, J. O. Dabiri, and J. D. Eldredge, *Lagrangian coherent structures in low Reynolds number swimming*, J. Phys.: Condens. Matter **21** (2009), 204105–4–204105–9.

87. E. Wolanski, *Hydrodynamics of mangrove swamps and their coastal waters.*, Hydrobiologia **247** (1992), 141–161.

88. J. Zhang, P. C. Johnson, and A. S. Popel, *Red blood cell aggregation and dissociation in shear flows simulated by lattice Boltzmann method*, J. Biomech. **41** (2008), 47–55.